Correspondence to:

L.-W. Kuo,
liweikuo@ncu.edu.tw;
liweikuo@gmail.com

Frictional Properties of the Longmenshan Fault Belt Gouges From WFSD-3 and Implications for Earthquake Rupture Propagation

Li-Wei Kuo[1,2] [ID], Chien-Cheng Hung[3] [ID], Haibing Li[4] [ID], Stefano Aretusini[5] [ID], Jianye Chen[6] [ID], Giulio Di Toro[5,7] [ID], Elena Spagnuolo[5] [ID], Fabio Di Felice[5] [ID], Huan Wang[4], Jialiang Si[4] [ID], and Hwo-Shuenn Sheu[8] [ID]

[1]Department of Earth Sciences, National Central University, Taoyuan, Taiwan, [2]Earthquake-Disaster & Risk Evaluation and Management Center, National Central University, Taoyuan, Taiwan, [3]Earth Simulation Laboratory, Department of Earth Sciences, Utrecht University, Utrecht, The Netherlands, [4]Key Laboratory of Deep-Earth Dynamics of Ministry of Natural Resources, Institute of Geology, Chinese Academy of Geological Sciences, Beijing, China, [5]Istituto Nazionale di Geofisica e Vulcanologia, Rome, Italy, [6]State Key Laboratory of Earthquake Dynamics, Institute of Geology, China Earthquake Administration, Beijing, China, [7]Department of Geosciences, University of Padua, Padua, Italy, [8]National Synchrotron Radiation Research Centrer, Hsinchu, Taiwan

Abstract The 2008 M_w 7.9 Wenchuan earthquake generated ∼270 and ∼80 km long surface ruptures along the Longmenshan fault belt, namely the Yingxiu-Beichuan fault (YBF) and the Guanxian-Anxian faults (GAF), respectively. So far, most of the frictional investigations were performed on the YBF gouge materials. Here, we present the results of rotary shear friction experiments performed on the GAF gouges recovered from the depth of ∼1.25 km of the Wenchuan Earthquake Fault Scientific Drilling project-3 along the GAF. The fault gouges, mainly composed of quartz, illite, chlorite, and kaolinite, were sheared at slip velocities V ranging from 10^{-5} to 2 m/s and normal stresses from 8.5 to 10 MPa under both room humidity and wet conditions. At any imposed slip velocity, the wet gouges have an apparent friction coefficient lower than the room humidity one. In addition, enhanced velocity-strengthening behavior at intermediate velocities (10^{-2} m/s $< V \leq 10^{-1}$ m/s) was recognized. We characterized the products using field-emission scanning electron microscopy combined with synchrotron X-ray diffraction analysis. These microanalytical investigations evidence the formation of size-reduced particles (without mineral phase changes) and R- and Y-shears in the principal slip zone (PSZ). Regardless of the ambient conditions, the width of PSZ was proportional to the input frictional work density (the product of shear stress times displacement). Our results support the hypothesis that the GAF preferentially ruptures through wet fault gouges; however, the enhanced velocity-strengthening regime at intermediate velocities may act as a barrier to slip acceleration during fault rupture propagation.

Plain Language Summary During the 2008 M_w 7.9 Wenchuan earthquake, two surface ruptures were generated, namely the ∼270 km long Yingxiu-Beichuan fault (YBF) and the ∼80 km long Guanxian-Anxian faults (GAF), respectively. This earthquake triggers mechanisms that weaken fault-zone rocks, allowing the rupture to propagate. While the frictional behavior of the YBF fault gouges and the possible mechanisms were investigated in detail, the GAF materials have not been studied yet. Here, we shear fault gouges of the GAF from low to high velocities and characterize the products. Results show that at any imposed slip velocity, the wet gouges are weaker than the room humidity ones. In addition, GAF fault gouges show high frictional resistance at intermediate velocities (10^{-2} m/s $< V \leq 10^{-1}$ m/s). The microanalytical investigations evidence the similarity between the experimentally formed principal slip zone and the reported natural observation of GAF fault gouges. Our results support the hypothesis that the GAF preferentially ruptures through wet fault gouges; however, the high frictional resistance at intermediate velocities may act as a barrier to slip acceleration during the 2008 Wenchuan M_w 7.9 earthquake.

1. Introduction

The Longmenshan fault belt located near SE-Tibet and bordering the western margin of the Sichuan basin in China, ruptured in the M_w 7.9 Wenchuan earthquake on 12 May 2008 (Liu-Zeng et al., 2009). The large in magnitude earthquake generated a ∼270 and ∼80 km long surface rupture along the Yingxiu-Beichuan fault (YBF) and the Guanxian-Anxian faults (GAF), respectively (Figure 1; Li et al., 2013; Xu et al., 2009). The GAF
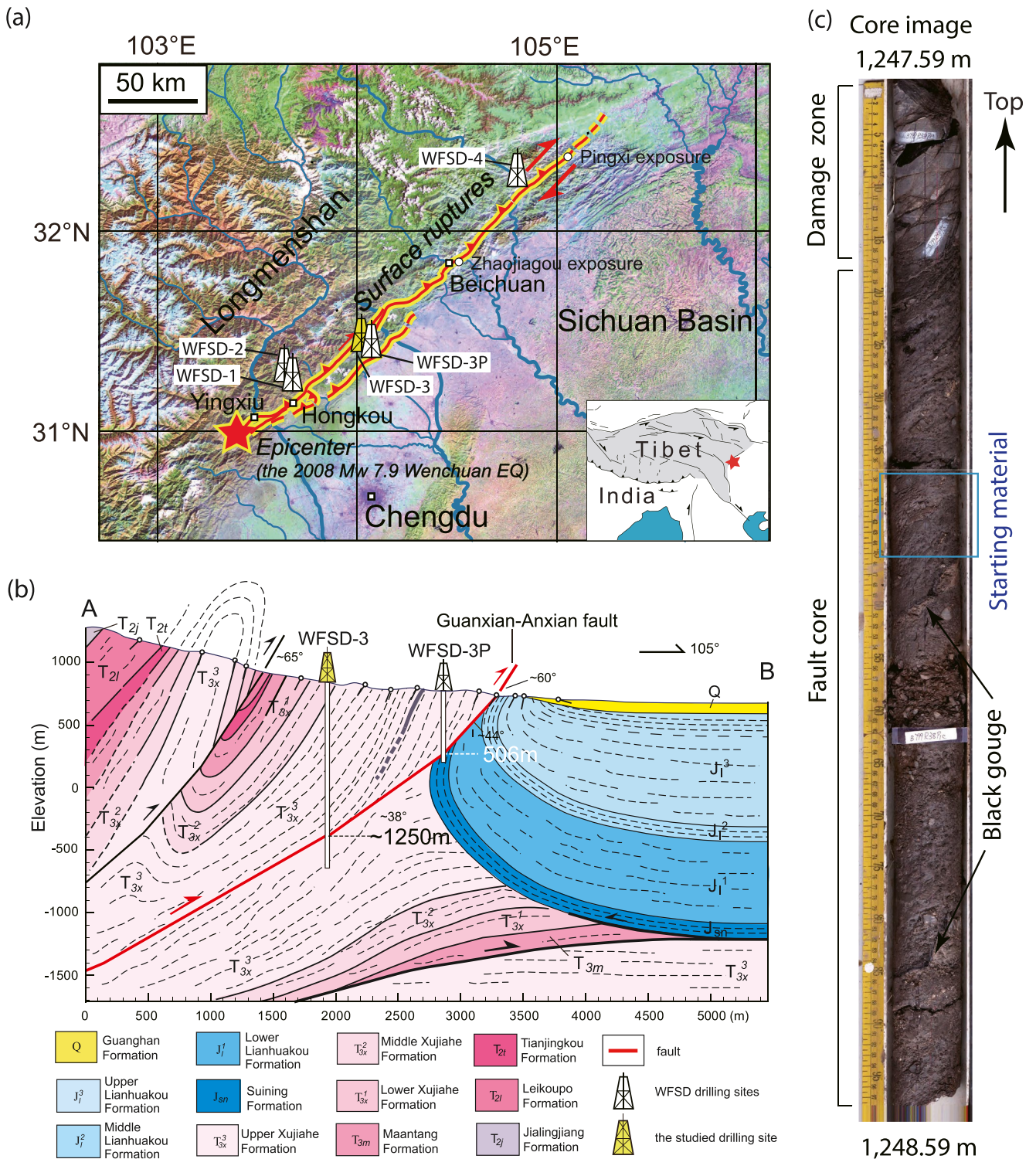
Figure 1. Geological setting of the 2008 M_w 7.9 Wenchuan earthquake and location of all the WFSD drilling sites. (a) Location of the WFSD-3 drilling site (marked in yellow) and the two surface ruptures associated with the M_w 7.9 earthquake along the margin of the Longmenshan mountain and Sichuan basin. The epicenter of the mainshock is marked as a red star. The inset box shows a schematic drawing of the Tibetan Plateau. (b) Cross-section of the WFSD-3 drilling site showing the GAF fault zone and surrounding formations encountered in the borehole (after Li et al., 2016). The possible fault zone activated during the 2008 mainshock rupture was assumed in the borehole at ~1,248 m depth and is plotted as the heavy red line. (c) The core image exhibiting the major portions of GAF along the borehole of WFSD-3. The gouge materials used in this study is marked in blue rectangle.

is sub-parallel and crops out 20 km east of the YBF. Seismic wave inversion analysis estimated a maximum fault displacement of ~7.3 m at an average slip rate of 1.25 m/s for this earthquake (Y. Zhang et al., 2009). In addition, field observations measured vertical coseismic surface offset. along the YBF and GAF of ~11 and ~4 m, respectively (Xu et al., 2009). The seismic energy radiated, the length of the surface rupture and the magnitude of coseismic slip make the 2008 Wenchuan M_w 7.9 earthquake the largest instrumentally recorded earthquake associated to a high-angle reverse fault within the continental interior (P. Z. Zhang et al., 2010). The integration of geological field surveys with data from the Wenchuan Earthquake Fault Scientific Drilling (WFSD-1) project and from seismic inversion showed that the YBF is a high-angle thrust fault striking NW with a dip angle of ~65° (Li et al., 2013). Instead, the interpretation of seismic inversions studies and the results of the WFSD-3 core analyses showed that the slip surface of the GAF is a thrust fault with a dip angle of ~38° (Li et al., 2015). The YBF and GAF have different fault-zone thicknesses in total (~100 and ~50 m, respectively), and fault structures (He et al., 2018; Li et al., 2013, 2015). In the two faults, the evolution of frictional strength and its associated dynamic weakening mechanism played a pivotal role in the determination of such large coseismic displacements.

Experimental studies to determine the frictional properties of both cohesive and non-cohesive (i.e., gouges) rocks at high velocities (≥0.01 m/s) commonly exploit rotary shear machines to achieve large displacements (a few meters; Di Toro et al., 2004; Ma et al., 2014; Mizoguchi et al., 2007; Reches & Lockner, 2010; Smith et al., 2013; Tsutsumi & Shimamoto, 1997). After the 2008 Wenchuan earthquake, high-velocity rotary shear experiments were conducted on natural gouges collected from different segments of the YBFs (Figure 1a), including (a) in the locality of Pingxi (Chen, Yang, Yao, Ma & Shimamoto, 2013; Yao, Ma, Shimamoto, & Togo, 2013; Yao. Shimamoto, et al., 2013), (b) in the locality of Zhaojiagou (Chen et al., 2017; Chen, Yang, Duan, Shimamoto, &Spiers, 2013; Hou et al., 2012), and (c) in the locality of Hongkou (Togo et al., 2011, 2016). In addition, after the accomplishment of the WFSD project, rotary shear experiments were also conducted on the drilling borehole materials (WFSD-1) along the YBF, for example, the gouge within the active fault zone (Kuo et al., 2017; Kuo, Li, et al., 2014; Togo et al., 2016). These experimental studies report dynamic weakening associated with frictional heating and suggest the activation of thermo-mechanical reactions (e.g., the graphitization of carbonaceous materials; Kuo, Li, et al., 2014, 2017).

While the frictional behavior of the YBF fault gouges and the possible associated "deformation" mechanisms were investigated in detail, the GAF materials have not been studied yet. To this end, we present here a suite of low- to high-velocity rotary shear experiments performed on fault gouges recovered from the WFSD project-3 (WFSD-3). The experiments were performed under room humidity and water-saturated (wet) conditions at imposed slip velocities V ranging from 10^{-5} to 2 m/s. The integration of the mechanical data with the microstructural analysis of the sheared materials allow us to produce a reference dataset of the frictional properties of the GAF materials and speculate about the deformation mechanisms associated to seismic faulting. Importantly, the microstructures produced in the experiments, which include the formation of principal slip zone (PSZ) and associated size-reduced particles and R- and Y-shears, are remarkably similar to the natural microstructures found in the WFSD-3P (He et al., 2018). The interpretation of the mechanical data suggest that flash heating and pore fluid thermo-mechanical pressurization likely operated in the GAF at shallow depth during the 2008 Wenchuan M_w 7.9 earthquake, even though the enhanced velocity-strengthening regime at intermediate velocities may act as a barrier to slip acceleration during fault rupture propagation.

2. Materials and Methods

2.1. Starting Materials

To investigate the physical processes associated with seismic faulting during the 2008 M_w 7.9 Wenchuan earthquake, four WFSD boreholes were conducted aimed at penetrating the Longmenshan fault belt at depth, including both the YBF and GAF (Figure 1a; Li et al., 2013, 2016). The WFSD-1 and WFSD-2 boreholes, located at ~40 km north-east of the epicentral area, were drilled in the YBF hanging wall. At 570 m depth of WFSD-1, the borehole passed from the Precambrian Pengguan complex (diorite, porphyrite, volcanic rocks, and pyroclastics) into the Triassic Xujiahe Formation (coal-bearing sandstones, siltstones, and shales), broadly marking the location of the Longmenshan fault zone. Based on the observations from the WFSD-1 and WFSD-2, it was inferred that seismic faulting along the YBF likely occurred in a fault dipping at high angle (~65°) at shallow depths (Li et al., 2013).
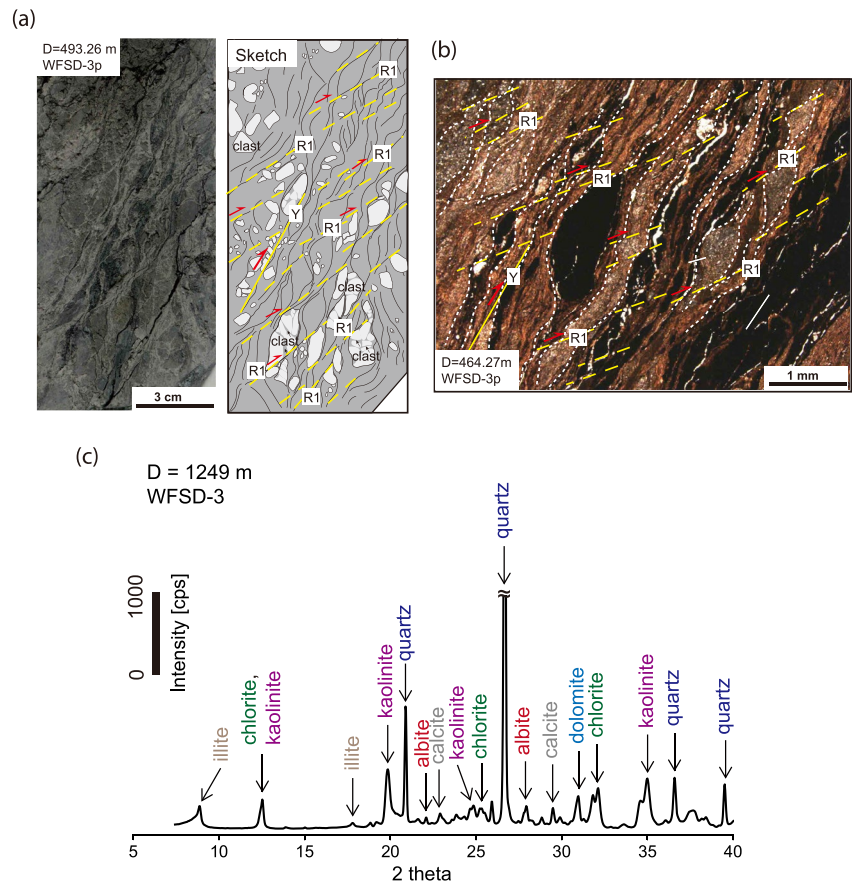
Figure 2. Images, microstructures, and mineralogical phases of the cores from the WFSD-3p. (a) The 493.26–493.41 m depths: foliated fault gouge with Y and P shears and distributed R1 shears, and some deformed clasts. Red half arrows indicate the shear directions and the red arrows show the compression direction (He et al., 2018). (b) Wavy boundaries between banded carbonaceous materials and clay-rich layers with distributed R1 shears. (c) Mineralogical phases of the materials used (at the depth of 1,249 of WFSD-3) for rotary shear experiment determined by in situ synchrotron X-ray diffraction analyses.

The pilot borehole WFSD-3P, located at ∼550 m northwest of the surface rupture along the GAF, was drilled in the GAF hanging wall to a depth of 551.51 m (Figure 1b). Integration of both the surface rupture and the core observation suggests that the active fault zone of the GAF likely was encountered at the depth of ∼507 m of WFSD-3P (He et al., 2018). The microstructures of the active fault zone of WFSD-3P showed the pervasive distribution of Riedel shears and pressure solution seams within numerous fine-grained clay-rich layers (Figures 2a and 2b).

WFSD-3 was located at ∼820 m northwest of WFSD-3P (Figure 1b). Drilling of the WFSD-3 was stopped at 788 and 1,096 m depth because of borehole collapse. Two sidetracks (WFSD-3-S1 and WFSD-3-S2) were drilled to reach the target depth of 1,500 m. Therefore, WFSD-3, WFSD-3-S1, and WFSD-3-S2 (named as WFSD-3 hereafter) reached 1,186.77, 788.00–1,187.28, and 1,096.00–1,502.3 m depth, respectively (Figure 4a in Li et al., 2016). The ∼1,500 m long borehole cores of the WFSD-3 are within the Triassic Xujiahe Formation (Figure 1b; Li et al., 2016). The interpretation of the logging data and the observation of the borehole cores showed five fault zones in the coring depth interval (Li et al., 2016). Based on the interpretation of the seismic reflection profiles across the GAF (Figure 2 in Li et al., 2016), the active fault zone was expected to be encountered at the depth of 1,100–1,300 m, including two of the five fault zones located at the 1,205–1,229 and 1,236–1,250 m (FZ1,250) depth, respectively.

The FZ1,250 is ∼14-m-thick, and, toward the bottom, includes a ∼1-m-thick fault core made by gray and black in color gouges (Figure 1c). Besides that, the detailed characterization of FZ1,250 is lacking. Here we simply
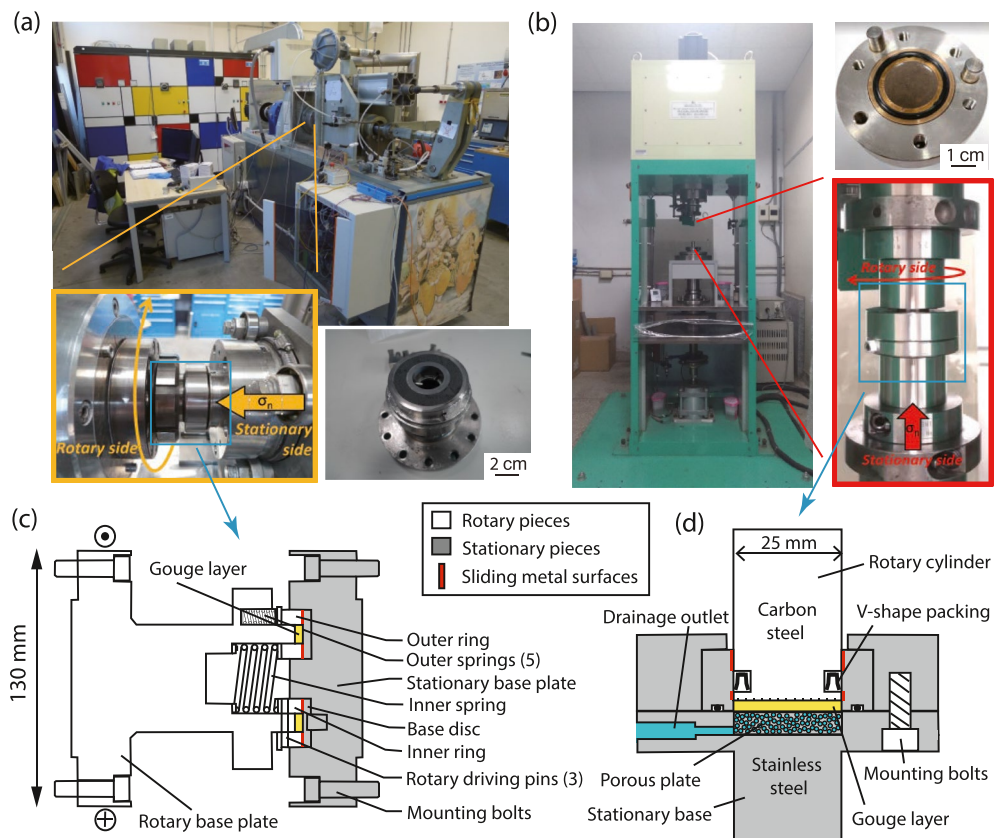
Figure 3. Two types of rotary shear apparatus used and the associated purpose-built sample holder. (a) SHIVA installed in INGV, Rome, Italy. Yellow rectangle showing the SHIVA equipped with the purpose-built sample holder. (b) LHVR installed at NCU, Taoyuan, Taiwan. Red rectangle displaying the LHVR equipped with the purpose-built sample holder. (c and d) Scale diagram of gouge holder showing rotary and stationary parts.

speculate the FZ1,250 as the possible active fault zone that ruptured during the 2008 Wenchuan earthquake (Li et al., 2016). We collected gray gouges from the depth of 1,248 m and adjacent to the black gouge as the starting material for the low-to high-velocity rotary shear experiments (Figure 1c). The gray gouge samples are composed of quartz (~55 wt.%), clay minerals (~32 wt.%: iolite, chlorite, and kaolinite), and minor albite (~8 wt.%), calcite, dolomite, and carbonaceous materials (<5 wt.%; Figure 2c).

2.2. Low-to High-Velocity Rotary Shear Experiments

Rock deformation experiments were conducted in the slow-to-high velocity apparatus (SHIVA) at the Istituto Nazionale di Geofisica e Vulcanologia (INGV, Rome), Italy (Figure 3a; Di Toro et al., 2010), and the low-to-high velocity rotary shear friction apparatus (LHVR) installed at the National Central University (NCU), Taiwan (Figure 3b; Kuo et al., 2015). Both the rotary shear machines are equipped with a metal sample holder for confining gouges (Figures 3c and 3d; Kuo et al., 2021; Smith et al., 2013). All rock deformation experiments were performed at room temperature and at normal stresses of 8.5–10 MPa under drained conditions (i.e., one atmosphere condition). Experiments were performed both under room humidity conditions (LHVR and SHIVA) and under water-saturated (wet) conditions (LHVR). After the experiment, we did not observe presence of extruded gouge from the vessel.

The gray gouge samples were first gently crushed and sieved to a grain size of <250 μm. For SHIVA, 5 g of gouge were poured into a ring-shaped (35 mm internal and 55 mm external in diameter) sample holder, resulting in an initial layer thickness of ~3 ± 0.4 mm (Figure 3a; Kuo, Li, et al., 2014; Smith et al., 2013). For LHVR, 2 g of gouge were mixed with water and poured into a disk-shaped (25 mm external in diameter) sample holder (see the detail in Kuo et al., 2021 for sample preparation). Before shearing, the gouge was first compacted by applying a normal load of 1 MPa and allowing for water drainage, and then pre-sheared by sliding at a slow slip

rate (1 mm/s) for ~10 s to suppress the pressurization effects due to gouge compaction (Faulkner et al., 2018). After the pre-shearing, the gouge was further compacted under a constant normal stress of 8.5 MPa until the axial displacement transducer recorded a constant value which was achieved in <1 hr. During compaction, pore water in the gouge layer was drained out through the fluid outlet. The initial thickness of gouge layer was ~2 ± 0.4 mm (Figure 3b; Kuo et al., 2021; the detailed process is described below), and the water content was ~26 wt.%. The initial thickness for the LHVR room humidity experiments was similar to the wet one. Both the stationary base and the rotary cylinder were etched with a cross-hatch pattern to provide roughness at the gouge-holder contact and inhibit slippage along this interface. Gouges (confined by the filter paper) were not extruded during compaction.

Both slip and slip velocity increase toward the outer radius of the gouge layer. We define the equivalent velocity V_e (Hirose & Shimamoto, 2005):

$$V_e = \frac{4\pi R \left(r_{ext}^2 + r_{ext} r_{int} + r_{int}^2 \right)}{3(r_{ext} + r_{int})} \left[\frac{m}{s} \right], \tag{1}$$

where R is the revolution rate of the motor. For LHVR, the target V_e is 1 m/s. Hereafter we refer to the "equivalent velocity" as the velocity V.

Both sample holders (i.e., the friction of the metal sample holder or spurious friction) contributed <30% torque in the range of normal stresses of 8.5–10 MPa (Kuo et al., 2021; Smith et al., 2013). Because the contribution to the measured torque from the sample holder was constant and slip rate independent, we reported the mechanical data without subtracting this contribution. In addition, we considered the mechanical data as apparent friction coefficient μ because pore fluid pressure within the slip zone was not measured, though pore fluid pressures and temperatures were modeled for few experiments, see Section 3.2.

We conducted 12 velocity-stepping and single (trapezoidal function) velocity experiments (Table 1). The velocity-stepping experiments were paused to reset the motor speeds to target values and then continued toward total displacements of 0.30–0.36 m for 10^{-5} m/s $\leq V \leq 10^{-2}$ m/s or of ~3 m for $0.05 \leq V \leq 0.5$ m/s. The single velocity experiments were performed at target V ranging from 100 μm/s to 2.0 m/s with total displacements of 0.5–1.2 m. In addition, for the single velocity experiments, the gouge samples were compacted at 1 MPa and pre-sheared at 1 mm/s with slip of 1 cm by either SHIVA or LHVR. Six experiments used gouges at room humidity (namely room humidity gouges hereafter) and the others used water-saturated gouges (namely wet gouges hereafter). Mechanical data were recorded at 10–1,000 Hz depending on the imposed velocities (Table 1). The experimental results are presented as the coefficient of friction to facilitate comparison between the experiments conducted with our two rotary shear machines. Aretusini et al. (2017) compared full and hollow cylinders gouge holders. Because the differences of data were small, they suggested that the evolution of friction coefficient is almost independent of the type of gouge holder used. This allows us to compare the mechanical data obtained with SHIVA with those with LHVR.

We introduce the frictional work density (FWD) and the frictional power density (FPD), representing the total work dissipated in the slip zone and the total power dissipated within the gouge layer (e.g., Aretusini et al., 2017; Di Toro et al., 2011), respectively. FWD and FPD can be defined as:

$$FWD = \int_0^X \tau(x)dx, \tag{2}$$

with X the total displacement and $\tau(x)$ the shear stress evolution with displacement x, and

$$FPD = FWD/\Delta t, \tag{3}$$

with Δt the duration of the experiment (Table 1).

The calculated FWD and FPD from the mechanical data will be correlated with the microstructure of the gouge layer described below.

2.3. Analytical Methods

After the single velocity experiments, the sheared gouges were dried out in an environmental chamber and impregnated with a low viscosity epoxy resin. Most microstructures may be disturbed by the drying methodology

Table 1
List of Experiments, Experimental Conditions, Mechanical Data, and the Thickness of Principle Slip Zone

Experiment	Ambient conditions	Slip velocity V (m/s)	Acceleration/ Deceleration (m/s²)	σ_n (MPa)	Total slip (m)	Peak τ_p (MPa)	Average steady state τ_{ss} (MPa)	Average steady state μ (-)	Range in steady state μ (MPa)	Frictional power density (MW/m²)	Frictional work (MJ/m²)	Slip weakening distance D_c (m)	PSZ width (mm)	Sampling rate (Hz)
LHVR1559	Room humidity	0.00001	3.5	8.7	0.01	–	2.88	0.33	0.05	0.00003	0.0288		0.9	10
LHVR1050	Room humidity	0.05	3.5	8.5	1.20	–	6.87	0.81	0.13	0.34350	8.2440		2.2	1000
s1126	Room humidity	1	6	8.8	1.00	3.74	2.29	0.26	0.02				–	25
s1127	Room humidity	2	23	8.7	0.50	3.73	1.18	0.14	0.05	2.35822	0.5896	0.2800	0.68	25
LHVR1056	Water saturated	0.00001	3.5	10.0	1.00	3.41	1.66	0.17	0.02	0.00002	1.6625		0.8	10
LHVR1045	Water saturated	0.05	3.5	8.5	1.20	–	5.05	0.59	0.03	0.25259	6.0620		1.97	1000
LHVR1037	Water saturated	1	3.5	8.5	7.00	3.58	0.80	0.09	0.16	0.79720	5.5804	0.50	–	1000
LHVR1558	Water saturated	1	3.5	8.7	0.90	3.16	1.55	0.18	0.03	1.55000	1.3950	0.45	0.49	1000
s1138														
Step 1	Room humidity	0.00001	23	9.9	0.01	4.35	3.74	0.38	0.00	0.00004	0.03315			25
Step 2	Room humidity	0.0001	23	9.9	0.03	–	4.34	0.44	0.00	0.00043	0.13023			25
Step 3	Room humidity	0.001	23	9.9	0.06	4.96	4.90	0.50	0.00	0.00490	0.29371			25
Step 4	Room humidity	0.01	23	10.1	0.15	5.62	5.26	0.54	0.01	0.05255	0.78831			25
Step 5	Room humidity	0.001	23	9.9	0.06	–	5.16	0.52	0.02	0.00516	0.30932			25
Step 6	Room humidity	0.0001	23	9.8	0.03	–	5.14	0.52	0.00	0.00051	0.15405			25
Step 7	Room humidity	0.00001	23	9.8	0.01	–	5.08	0.52	0.01	0.00005	0.05075			25
LHVR1044														
Step 1	Room humidity	0.05	3.5	8.5	0.50	–	6.27	0.74	0.13	0.31325	3.13250			1000.00
Step 2	Room humidity	0.1	3.5	8.5	0.50	–	6.15	0.72	0.08	0.61510	3.07550			1000.00
Step 3	Room humidity	0.2	3.5	8.5	1.00	–	5.00	0.59	0.14	1.00080	5.00400			1000.00
Step 4	Room humidity	0.5	3.5	8.5	1.50	–	4.51	0.53	0.06	2.25500	6.76500			1000.00
LHVR1027														
Step 1	Water saturated	0.00001	3.5	10.0	0.01	–	3.01	0.30	0.02	0.00003	0.03008			25
Step 2	Water saturated	0.0001	3.5	10.0	0.03	–	3.30	0.33	0.03	0.00033	0.09904			25
Step 3	Water saturated	0.001	3.5	10.0	0.06	–	3.73	0.37	0.08	0.00373	0.22408			25
Step 4	Water saturated	0.01	3.5	10.0	0.15	–	5.16	0.52	0.03	0.05160	0.77399			25
Step 5	Water saturated	0.001	3.5	10.0	0.06	–	4.88	0.49	0.03	0.00488	0.29298			25
Step 6	Water saturated	0.0001	3.5	10.0	0.03	–	4.06	0.41	0.01	0.00041	0.12165			25
Step 7	Water saturated	0.00001	3.5	10.0	0.01	–	3.92	0.39	0.02	0.00004	0.03920			25

Table 1
Continued

Experiment	Ambient conditions	Slip velocity V (m/s)	Acceleration/ Deceleration (m/s²)	σ_n (MPa)	Total slip (m)	Peak τ_p (MPa)	Average steady state τ_{ss} (MPa)	Average steady state μ (-)	Range in steady state μ (MPa)	Frictional power density (MW/m²)	Frictional work (MJ/m²)	Slip weakening distance D_c (m)	PSZ width (mm)	Sampling rate (Hz)
LHVR1046														
Step 1	Water saturated	0.05	3.5	8.5	0.50	–	4.61	0.54	0.10	0.23025	2.30250			1000.00
Step 2	Water saturated	0.1	3.5	8.5	0.50	–	4.61	0.54	0.04	0.46080	2.30400			1000.00
Step 3	Water saturated	0.2	3.5	8.5	1.00	–	3.53	0.42	0.14	0.70600	3.53000			1000.00
Step 4	Water saturated	0.5	3.5	8.5	1.50	–	1.21	0.14	0.05	0.60550	1.81650			1000.00

(i.e., shrinkage may occur) either or after shear deformation (Aiyama et al., 2019). The impregnated samples were prepared into 30 μm thick petrographic thin sections, cut across the diameter of the sample and perpendicular to the slip surface. The thin sections were coated with platinum to increase the electrical conductivity for scanning electron microscopy analysis. In addition, the thin sections were analyzed with in situ synchrotron X-ray diffraction (XRD) for bridging microstructural and mineralogical observations (e.g., Hung et al., 2019; Wu et al., 2020).

We utilized field emission scanning electron microscopy, coupled with an energy dispersive spectrometer (FESEM/EDX; JSM-7000F model) at the National Central University, Taiwan. The FESEM was operated at 15 kV acceleration voltage and 2.8×10^{-4} Pa vacuum. We used the in situ synchrotron XRD installed at the beamline BL01C2 in the National Synchrotron Radiation Research Center, Taiwan. The X-ray wavelength was 0.5166 Å delivered by a double crystal monochromator with two Si(111) crystals and transferred the wavelength of 0.5166–1.540 Å (CuKα) for the later data processing. The analyses were operated with an electron beam energy of 1.5 GeV and a beam size of 150 μm in diameter (e.g., Kuo, Hsiao, et al., 2014). To reduce the intensity anomalies derived from heterogeneous mineral assemblage distribution within the slip surface, the synchrotron XRD spectra were reported as the average values of three analyses along the same horizon of the same sample (Kuo et al., 2015).

3. Results

3.1. Frictional Behavior

The results of representative experiments from low to high velocities (10^{-5} m/s $\leq V \leq 2$ m/s) are reported in Figure 4. In velocity-stepping experiments (10^{-5} m/s $\leq V \leq 10^{-2}$ m/s and 0.05 m/s $\leq V \leq 0.5$ m/s, Figures 4a–4d) μ did not achieve "steady state" values. Therefore, we plot the average μ for a given velocity step, with the error bars representing the range in μ during the velocity step (Figure 5). The mechanical results of "steady state" μ are summarized in Figure 5 where data for room humidity and wet conditions are reported as a function of slip velocity. In single velocity experiments (Figures 4e–4j) we calculate the average steady state μ over a slip interval of ∼0.4 m (see box in Figure 4), with the error bars representing the range in μ within the slip interval (Figure 5).

In general, wet gouges are weaker than room humidity gouges at all investigated velocities (Figures 4 and 5). At low velocities ($V \leq 10^{-2}$ m/s), room humidity gouges have μ between 0.33 and 0.50, while μ for wet gouges is 0.17–0.49. At intermediate velocities ($10^{-2} < V \leq 10^{-1}$ m/s), in room humidity gouges μ increases up to 0.81, while in wet gouges up to 0.59. At high velocities ($V > 0.1$ m/s), the friction coefficients of both room humidity and wet gouges decrease to 0.09–0.18. In the single velocity experiments for $V \geq 1$ m/s, during deceleration at the end of slip, re-strengthening of both room humidity and wet gouges occurs, resulting in a final μ slightly higher than the steady state one (Figures 4i and 4j). In Figure 5, both room humidity and wet gouges exhibit velocity-neutral to -strengthening behavior for $V \leq 10^{-3}$ m/s, enhanced velocity-strengthening behavior $10^{-2} < V \leq 10^{-1}$ m/s and pronounced velocity-weakening behavior for $V > 0.1$ m/s (Figure 5).

3.2. Microstructure of the Sheared Gouges

3.2.1. Optical Microscope

To examine the textural evolution of the WFSD-3 gouges with imposed velocity and displacement, we characterize the microstructures produced in the single velocity experiments which are stopped once the steady state friction coefficient is reached (i.e., room humidity vs. wet experiments from low to high V). The representative microstructures of both the starting material and the sheared gouges are shown in Figure 6. Under cross-polarized light, the starting compacted WFSD-3 gouges have randomly oriented angular to sub-rounded clasts of quartz and minor plagioclase and calcite immersed in a yellowish in color clay-rich matrix (Figure 6a).

Independently of environmental conditions (room humidity vs. wet) and cumulative displacement, at the end of the experiments the gouge is dark brownish close to the rotary cylinder, while close to the stationary side is yellowish and similar to the starting material (Figures 6b–6g). The dark brownish
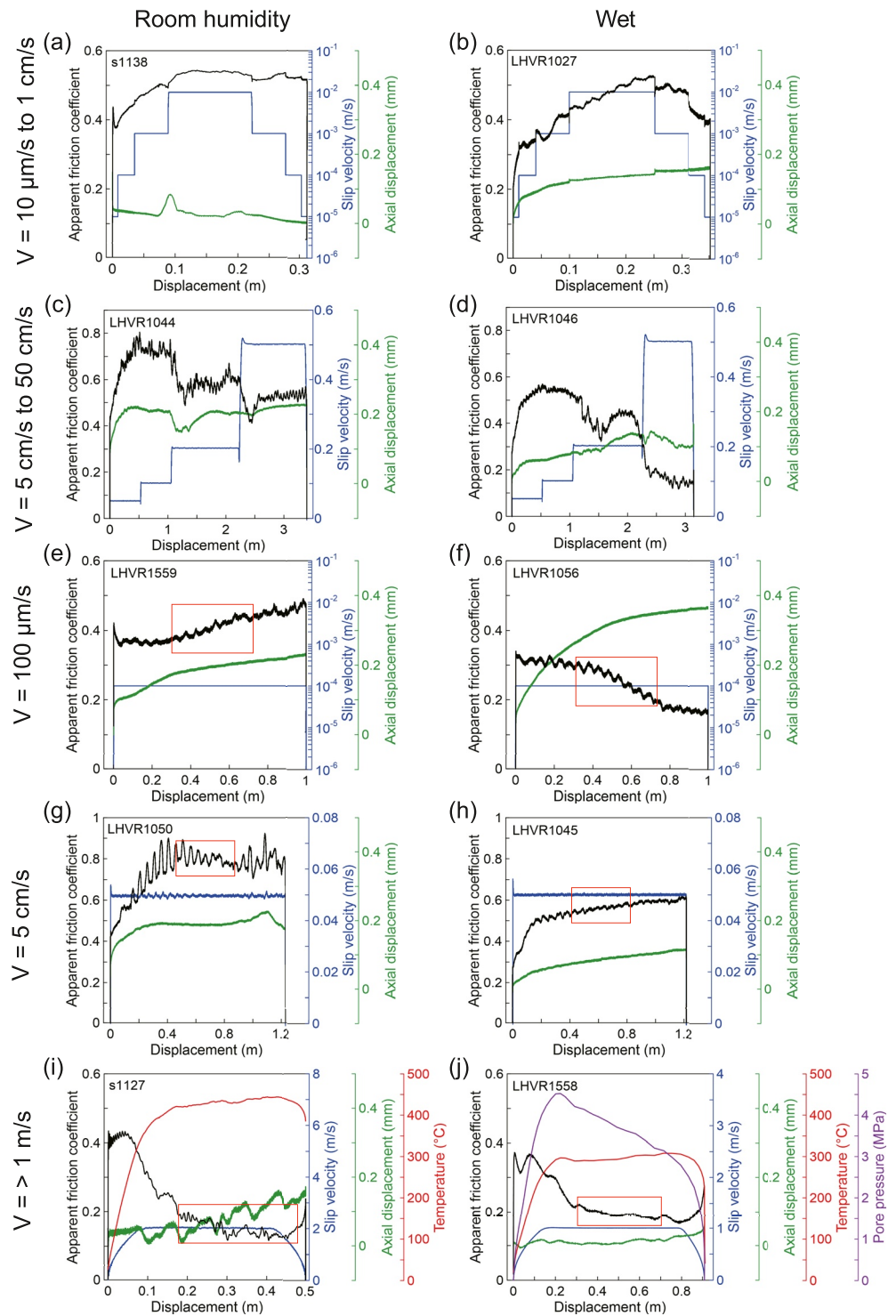
Figure 4. Friction coefficients of WFSD-3 gouges as a function of slip distance. (a–d) Slip stepping experiments. (e–j) Single velocity experiments. Red rectangles as the interval for the estimate of average friction coefficient of the gouge samples.

gouge includes rounded fine clasts wrapped by the clay-rich matrix and is here referred as the PSZ (Figures 6b–6g). The matrix of the PSZ is isotropic under cross-polarized light, and has an irregular contact, with local mixing, with the yellowish gouge (Figure 6). Some open fractures form sub-parallel to the gouge layer boundaries.
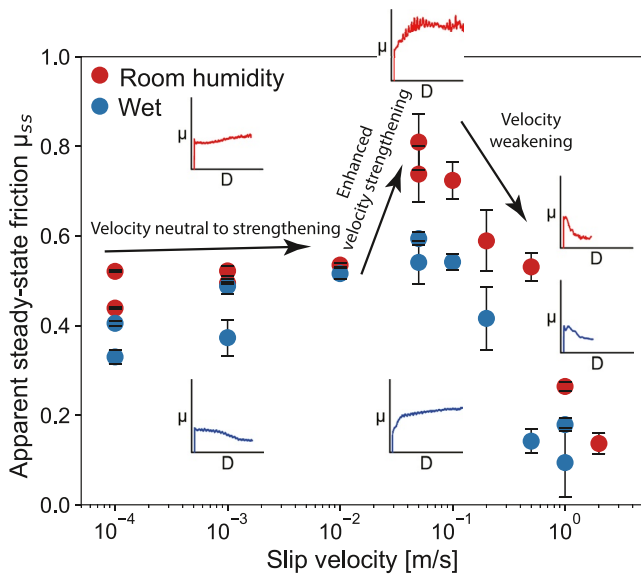
Figure 5. Friction coefficients of WFSD-3 gouges as a function of slip velocity. Each data point is averaged from multiple data points with standard deviation represented by error bars. Room humidity runs in red circles. Wet runs in blue circles. Insets report for reference the evolution of μ with displacement for room humidity (red line) and wet (blue line) runs.

3.2.2. Scanning Electron Microscope

The microstructure of the starting materials after compaction and pre-shear includes angular to sub-rounded clasts of quartz and plagioclase with grain size ranging from 10 to <250 μm, randomly distributed within the clay matrix (Figure 7a). Close to the rotary cylinder, the grain size of clasts decreases to few micrometers. The reduction in grain size is due to comminution at the boundary with the metal holder during pre-shear (Figure 7b).

Irrespective of environmental conditions and cumulated displacement, a continuous layer of PSZ forms the gouge/cylinder interface. The microstructure of PSZ is homogeneous, with rounded to sub-rounded clasts of quartz and feldspar immersed in the submicron-clay-rich matrix (Figures 7c–7h). In places, the PSZ is cut by Y or R shears (see definition in Logan et al., 1992).

We assessed the widths of PSZ (measured and averaged along the entire thin section length) with the error bars representing both the range of mixing region and the variation across the thin section of the gouge layer. Regardless of the environmental conditions, the width of PSZ is <1 mm thick at both low ($V \leq 100$ μm/s) and high ($V > 1$ m/s) velocities, and ~2-mm-thick at intermediate velocities (5 mm/s; Table 1). The measured widths of the PSZ are plot versus both FWD and FPD (Figure 8).

3.3. Mineralogy of the Sheared Gouge Layer

We conducted *in situ* synchrotron XRD analyses to determine the mineral assemblages of the PSZ in the thin sections (e.g., Kuo, Hsiao, et al., 2014; Kuo, Li, et al., 2014). The intensity of X-ray spectrum includes both minerals and glass because of the penetration of X-rays through the minerals and in the thin section beneath (Figure 9a). Therefore, to remove the contribution of the thin section from the bulk XRD spectrum, we first collected the spectrum of the glass (i.e., thin section itself) adjacent to the sample (background intensity) and, by assuming a constant thickness of the thin section, we subtracted the glass spectrum from the obtained sample spectrum. Then, we compared the XRD (powders) spectrum of the starting materials (Figure 2c) with the spectra (thin sections) of the experimental products from the single velocity experiments. The *in situ* synchrotron XRD analyses has ca. 1 wt.% detection limit.

The beam size of synchrotron XRD analyses is 150 μm in diameter. The width of PSZ varies from 0.2 to 2 mm based on the SEM observations. Therefore, the XRD spectra are related to the mineral assemblage of the PSZ. In all cases (both room humidity and wet conditions experiments), the investigated areas of PSZ and the starting material are composed of quartz, clay minerals, and minor albite, calcite, dolomite, and carbonaceous materials (Figures 9b and 9c). No new phases are recognized in the post-experiment samples, nor increase of the background signal, which may suggest the absence of amorphous material. *In situ* synchrotron XRD analyses shows the similarity of the mineral assemblages between the starting materials and the experimental products, independently of the imposed loading, environmental conditions, and velocities (Figures 9b and 9c). It is notable that all the intensity of XRD peaks at $V = 5$ cm/s are smaller than the ones from both low ($V = 100$ μm/s) and high ($V > 1$ m/s) velocities.

4. Discussion

### 4.1. Comparison to Previous Experimental Observations

To our knowledge, there is lack of experimental studies on the frictional properties of GAF gouges. Below we compare our mechanical data to previous results of experiments performed on similar mineral assemblages (mixtures of quartz and clay minerals, e.g., illite and chlorite,Table 2). It is notable that our results at low V show either slip weakening or strengthening with an increase of displacement in the experiments (Figures 4a, 4b, 4e and 4f). The friction coefficient data we obtained at low V but large displacements (i.e., >0.3 m) should be compared with caution with friction data from the literature obtained in small displacement (<0.01 m) experiments (e.g., Ikari et al., 2009; Moore & Lockner, 2004; Tembe et al., 2010). In general, our results are consistent
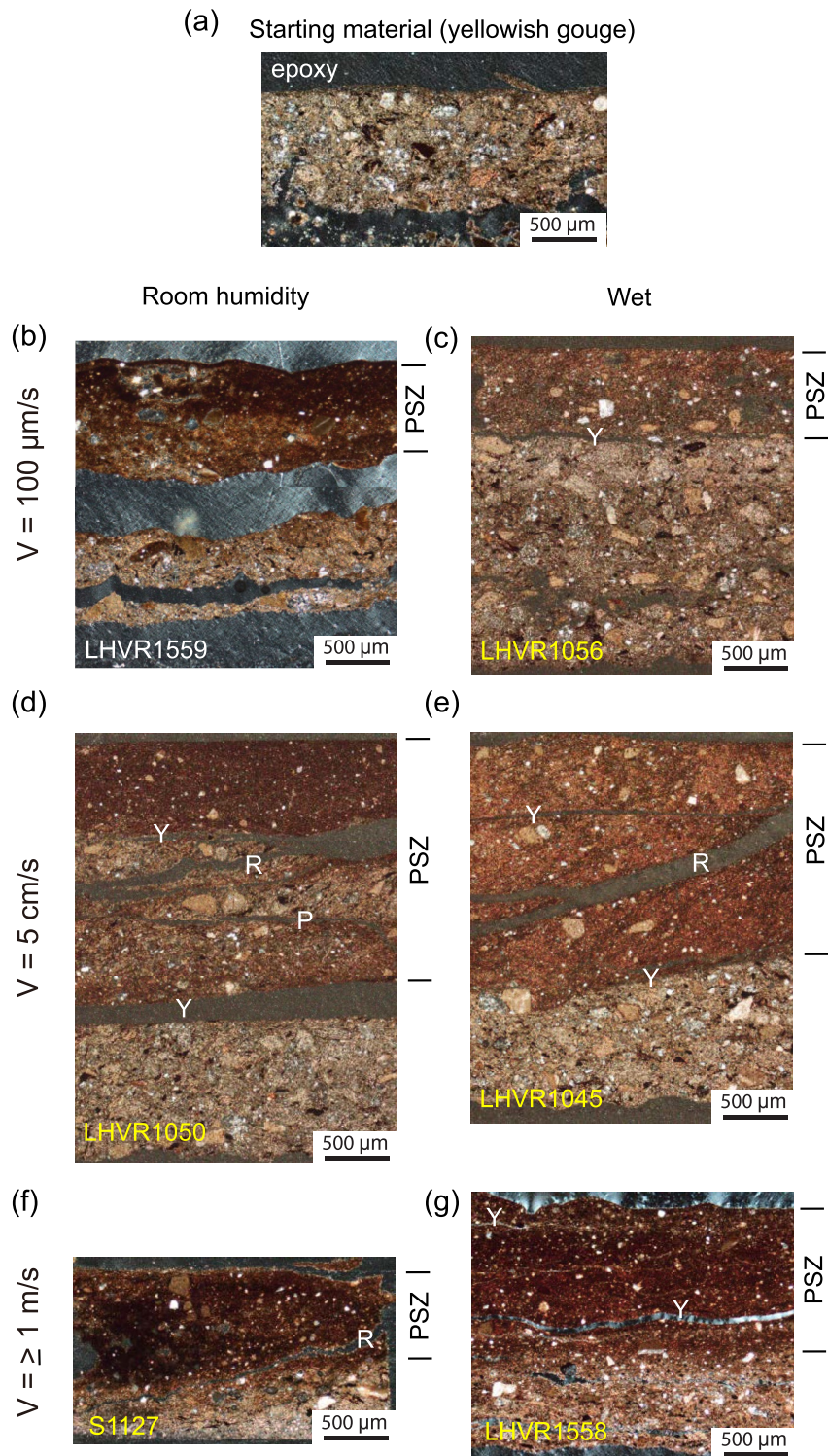
Figure 6. Cross-polarized light observation of the experimental products formed before (a) and after room humidity (b, d, and f) and wet (c, e, and g) experiments. Fault gouge composed of localized size-reduction particle zone and random distribution of clasts in optically isotropic, dark matrix.

with the previously published friction data on clay-rich gouge materials, but our dataset includes more experiments performed at high normal stress (up to 10 MPa; Table 2) in the intermediate to high velocity regimes (i.e., $V > 10^{-2}$ m/s).
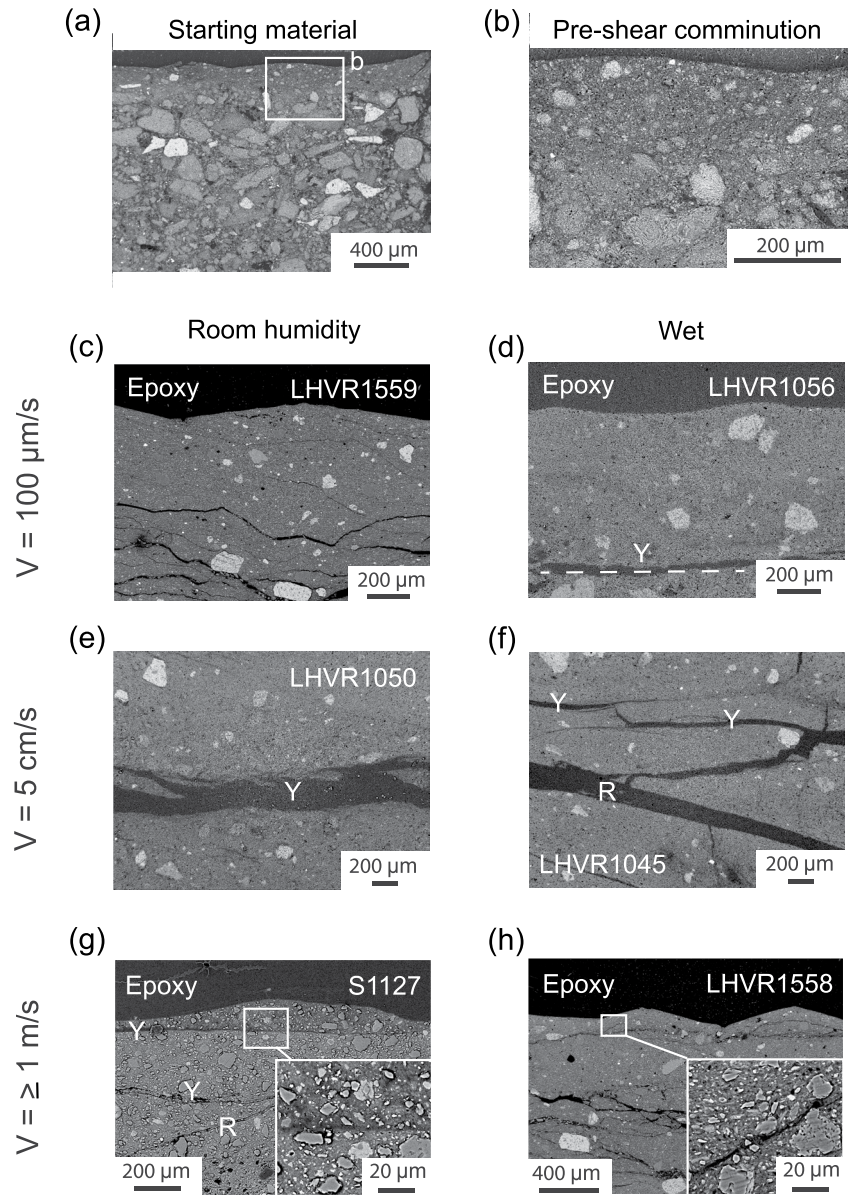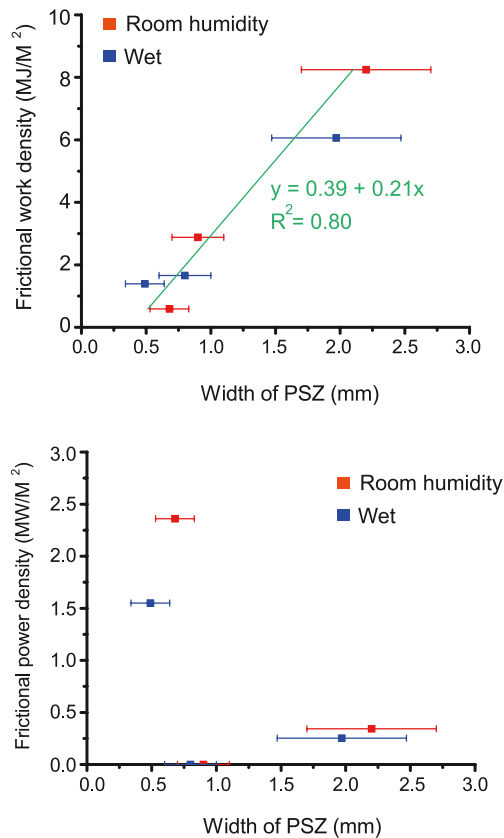
Figure 7. Backscattered SEM image of the sheared gouge layer cut through part of the localized size-reduction particle zone. Those images are from starting material after preshear (a, b), and under room humidity (c, e, and g) and wet (d, f, and h) experiments.

4.1.1. Data From Low Velocity Experiments ($V \leq 10^{-2}$ m/s)

At a normal stress of 10 MPa, the powdered WFSD-3 gouges have μ of 0.38–0.52 and 0.30–0.41 under room humidity and wet conditions, respectively. This is consistent with experimental data of similar in composition gouges (Ikari et al., 2007; Moore & Lockner, 2004; Morrow et al., 2000), according to which water saturation of phyllosilicate minerals reduces frictional strength by as much as 60%.

Ikari et al. (2009) preformed double direct shear experiments on powdered samples of illite shale and chlorite schists under water-saturated conditions. Ikari et al. (2009) sheared these gouges under an effective normal stress of 12 MPa and at velocities from 10^{-6} m/s to 3×10^{-4} m/s and reported μ of 0.29 (illite shale) and 0.32 (chlorite schists), respectively. These μ values overlap with the lower μ value of 0.30 measured under wet and similar loading conditions for our WFSD-3 gouges, which have a similar mineralogical assemblage. Brown et al. (2003) performed ring-shear seawater-saturated experiments on both mineral standards and natural clay-rich samples

Figure 8. PSZ width as function of (a) frictional work density (FWD) and (b) frictional power density (FPD). Error bars indicate the variation of PSZ width along the observed petrographic thin section.

from subduction thrusts. They reported a μ value of 0.42 for illite/quartz mixtures sheared under an effective normal stress of <2 MPa and at velocities of 1.5×10^{-6} m/s; this μ value overlaps with the higher μ value of 0.41 measured under wet and similar loading conditions for our WFSD-3 gouges.

Tembe et al. (2010) reported friction data obtained in triaxial compression tests according to which the friction coefficient decreased linearly with increasing clay content for illite/quartz mixture. For their synthetic 2-mm-thick wet sample of illite and quartz, they reported μ of 0.55 and 0.44 for 25% and 50% of illite, respectively, with the displacement of 9 mm slip. Based on the result of Tempe et al. (2010), an estimate of μ for illite content ~32% (in our study) was about 0.52 and is significantly higher than our observations. Mizoguchi et al. (2008) performed saw-cut triaxial compression friction experiments on borehole core samples stem from >1 km depth in the Taiwan Chelungpu fault Drilling Project (TCDP), Taiwan. The TCDP clay-rich gouge samples (namely 1134HR, 1136BZ, 1194BGZ, and 1243BGZ in their study) were qualitatively described as rich in quartz, illite and chlorite (Figure 3 in Mizoguchi et al., 2008). For these clay-rich gouges they reported μ of 0.38–0.52 at an effective normal stress of 14 MPa and velocities of 10^{-6}–10^{-5} m/s; two likely explanations for this difference is either jacketing (for triaxial compression experiments) and apparatus effects that cause strain hardening in the triaxial experimental configuration (Moore & Lockner, 2004), or the slip weakening behavior that the values of friction coefficient were obtained after dozens of centimeter of displacement in the experiments (Figures 4a, b, 4e and 4f).

Tanikawa and Shimamoto (2009) performed double direct shear experiments on clay-rich fault gouge from 286 m depth in the northern borehole of the Chelungpu fault, Taiwan. The clay-rich fault gouge was qualitatively described as a material rich in quartz, illite, and chlorite (in their Figure 3a). They reported μ for the clay-rich gouge of ~0.70 and 0.30–0.38 under room humidity and wet conditions, respectively, when sheared at a normal stress of 14.6 MPa and velocities of 1.5×10^{-7}–1.5×10^{-4} m/s. The μ measured in our "wet" experiments (0.30–0.41) are consistent with the μ values measured in their "wet" experiments. However, in our experiments performed under room humidity and similar loading conditions, the μ values are significantly lower (e.g., 0.38–0.52, Figure 5). This discrepancy could be related to the higher quartz content in the gouge samples from the Chelungpu fault.

4.1.2. Data From Intermediate Velocity Experiments ($10^{-2} < V \leq 10^{-1}$ m/s)

Below we compare our data with experimental data obtained with rotary shear-type experimental machines, commonly used to shear solid rocks and gouges at intermediate to high velocities (e.g., Mizoguchi et al., 2007; Tsutsumi & Shimamoto, 1997).
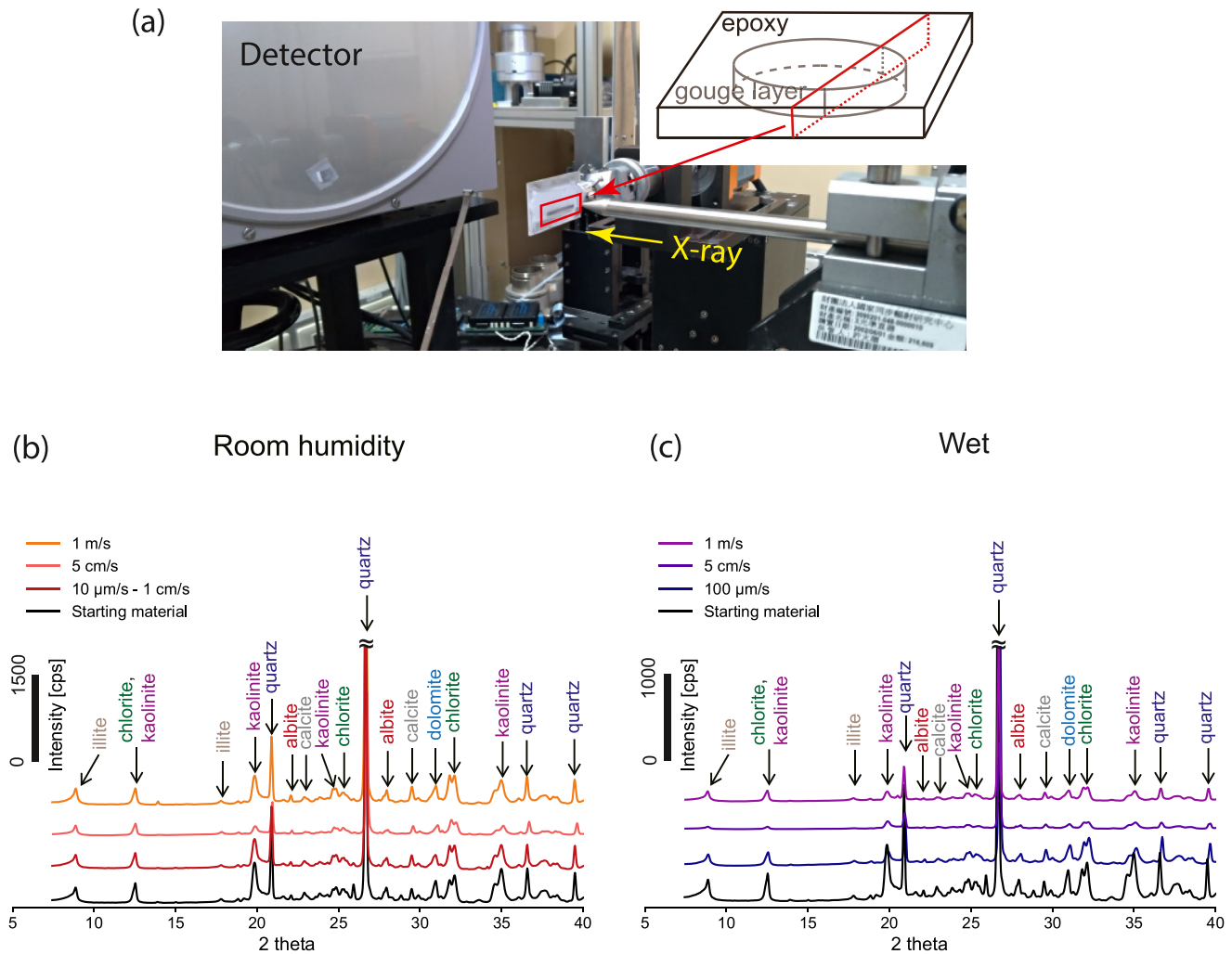
At intermediate velocities, the μ of the powdered WFSD-3 gouges increases with velocity from 0.50 to 0.81 and from 0.37 to 0.59 under room humidity and wet conditions, respectively. This velocity-strengthening behavior is consistent with results from previous experiments performed on clay-rich gouges (e.g., Ferri et al., 2011; Remitti et al., 2015). Ferri et al. (2011) conducted both velocity-stepping and single velocity experiments on clay-rich gouges (60%–70% Ca-smectite and 30%–40% of calcite and minor quartz) from the Vaiont landslide slip zone under room humidity conditions in this intermediate velocity regime. They reported that room humidity gouges exhibit velocity-strengthening behavior with μ increasing from 0.49 to 0.79 at an imposed velocity approaching 0.04 m/s. Our μ values for the clay-rich gouges sheared under room humidity conditions are consistent with their data though the mineral assemblages of the studied materials are different.

Remitti et al. (2015) conducted both velocity-stepping and single velocity experiments with SHIVA on smectite-rich gouges from the J-FAST drilling project (Tohoku 2011 M_w 9.0 earthquake) under room humidity and water-dampened conditions, respectively. They reported that the water-dampened gouges were extremely weak

Figure 9. In situ synchrotron X-ray analyses of a gouge layer. (a) The petrographic thin section situated on the sample holder of synchrotron holder (right panel of Figure 11a). (b and c) Mineralogical phase of the selected area within the gouge layer. cps, counts per second. The peaks confirm that similarity between the sheared gouge layers and the starting materials.

with μ around 0.05. In contrast, room humidity gouges exhibited velocity-strengthening behavior with μ increasing to 0.3–0.35 at a velocity approaching 0.1 m/s. The trend of increasing μ values with increasing velocity measured in our experiments (Figure 5) is consistent with their observations, though our μ values are systematically and significantly higher (up to 0.8) than their reported values. The higher values of μ are likely due to the higher abundance of quartz in the WFSD-3 gouge samples and to the presence of the weaker Na-smectite in the J-FAST gouges. The aforementioned reported mechanical data suggests that our observed velocity-strengthening behaviors at the intermediate velocities are universal.

4.1.3. Data From High Velocity Experiments (10^{-1} m/s < V)

Our data show a dramatic drop of μ from 0.81 to 0.14 and 0.59 to 0.01 with increasing slip velocities under room humidity and wet conditions, respectively. The measured μ at seismic rates is consistent with results from the aforementioned works and many others (see Di Toro et al., 2011). For example, Ferri et al. (2011) reported μ of ~0.14 and 0.01 under room humidity and wet conditions, respectively, for gouges sheared at a normal stress of 1 MPa and a velocity of 1.3 m/s Remitti et al. (2015) reported μ of ~0.12 to 0.16 and 0.07 under room humidity and water-dampened conditions, respectively, for gouges sheared at normal stresses of 3.53–8.39 MPa and velocities >1 m/s. Their reported mechanical data also showed a dramatic drop of μ with an increase of slip velocities.

Table 2
The Previous Results of Experiments Used for Comparison

	Low slip rate	Intermediate slip rate	High slip rate
Room humidity condition	0.30–0.38 (14 MPa; Tanikawa & Shimamoto, 2009)		0.10 (0.56 MPa; Sone & Shimamoto, 2009)
		0.49–0.79 (1 MPa; Ferri et al., 2011)	0.14 (1 MPa; Ferri et al., 2011)
		0.30–0.35 (~8.5 MPa; Remitti et al., 2015)	0.12–0.16 (8.2–12.4 MPa; Remitti et al., 2015)
		0.60 (0.56 MPa; Sone & Shimamoto, 2009)	0.20–0.30 (0.6–0.9 MPa; Tanikawa & Shimamoto, 2009)
			0.30 (~0.6 MPa; Boutareaud et al., 2008)
Wet condition	0.29–0.32 (25 MPa; Ikari et al., 2009)		
	0.42 (<2 MPa; Brown et al., 2003)	<0.10 (1 MPa; Ferri et al., 2011)	0.01 (1 MPa; Ferri et al., 2011)
	0.44–0.55 (40 MPa; Tembe et al., 2010)	0.05 (~3.5 MPa; Remitti et al., 2015)	0.07 (~3.5 MPa; Remitti et al., 2015)
	0.38–0.52 (14 MPa; Mizoguchi et al., 2008)		0.19 (~0.6 MPa; Boutareaud et al., 2008)
	0.30–0.38 (14 MPa; Tanikawa & Shimamoto, 2009)		

Regarding single-velocity experiments, Boutareaud et al. (2008) reported that μ of clay-rich gouge (mainly quartz and feldspar with minor phases of calcite, kaolinite, and illite-smectite mixed layers) from the Usukidani fault, Japan, was of ~0.30 and 0.19 under room humidity and wet conditions, respectively, when sheared at a normal stress of 0.6 MPa and a velocity of 1.3 m/s. Tanikawa and Shimamoto (2009) reported that μ of clay-rich fault gouges from the boreholes of the Chelungpu fault, Taiwan, was of ~0.20 to 0.30 when sheared under room humidity conditions at normal stresses of 0.6–0.9 MPa and a velocity of 1.06 m/s Sone and Shimamoto (2009) reported that μ of clay-rich fault gouge from the deep borehole of the Chelungpu fault, Taiwan, decreased from ~0.60 to 0.10 with an increase of slip velocities (0.1–2 m/s) under room humidity at normal stresses of 0.56 MPa. Our μ are lower than their reported values. This discrepancy could be related to (a) the different amount and mineralogy of the clays; (b) the larger normal stress applied in the experiments, which would result in lower dynamic friction coefficient (Kuo et al., 2021); and (c) the possibility of more intense compaction and fluid pressurization.

4.2. Mechanisms of Deformation in the Three Friction-Velocity Regimes

The friction coefficient of the WFSD-3 samples evolves with increasing velocity and water content, suggesting the activation of either strengthening or weakening mechanisms at different friction-velocity regimes. Below, we will propose deformation mechanisms active at different friction-velocity regimes. The interpretation is based on the combination of both mineralogical and microstructural observations, and on the estimate of the temperature and pore fluid pressure evolution in the PSZ in the high velocity regime.

The frictional strength of room humidity WFSD-3 gouges is systematically higher than the one of wet gouges at any investigated slip velocity (Figures 4 and 5). WFSD-3 gouges are made of quartz, illite, chlorite, and kaolinite which do not have interlayer water, so water is likely present (adsorbed) as a thin film on the grain surfaces. Schuttlefield et al. (2007) estimated about 10–75 mg water/g kaolinite and 150–225 mg water/g illite at 50%–60% relative humidity. We verified this range of adsorbed water in room humidity experiments of our powders (<1 wt.%) and found that the weight difference of water between ambient room condition (~50% humidity) and water-saturation condition (~26 wt.%) is larger than 25%. We envision that the water saturation state is the dominant controlling parameter of gouge shear strength leading to the contrasting behavior features between room humidity and wet WFSD-3 gouge samples (Figures 4 and 5), and also discuss the water-related weakening mechanisms below.

4.2.1. Velocity Neutral to Strengthening Behavior at Low Velocities

Both the mineral phases determined and the microstructures observed in the three friction-velocity regimes indicate the occurrence of cataclasis (grain comminution) and possibly shear along Y-shears (Figures 6, 7 and 9). The

obtained curves of axial displacement (compaction; Figure 4) are typical for loading and shearing of materials with the occurrence of cataclastic process (Niemeijer et al., 2010). This interpretation is supported by the fact that the observed compaction rates decrease with increasing slip distance (or time) because of porosity reduction by cataclastic process.

In the room humidity gouge samples the initial shear deformation is likely accommodated by slip at the contact between grains or along the basal planes of clay minerals, similarly to wet gouge samples (Figures 6 and 7). Because of the experimental configuration (e.g., Rempe et al., 2017), cataclastic processes and shear localization occur at the contact with the rotary side and results in grain size reduction. Comminuted grains form also during the initial pre-shear stage of the experiment (Figure 6b). The reduction of grain size increases the probability of interaction of grain edges between neighbor clasts and facilitates the redistribution of gouge materials, leading to the increase of grain contact area and the associated slip strengthening behavior. With progressive slip, the cataclastic processes continue and subsequently leads to the formation of a through-going horizontal shear (Y-shear), located near the shear zone boundary. All deformation likely localized into this Y-shear. Because quartz particles are embedded in the clay matrix, they act as high-strength "barriers" for the development of thoroughgoing R-shear within the clays. In addition, in the absence of evidence for quartz precipitation, the activation of pressure solution processes seems unlikely (Bos et al., 2000). This implies that a significant contribution of intergranular slip within the PSZ should indeed occur.

The progressively increasing frictional strength of the gouge suggests the increase of grain contact area, prevent localization and cause more pervasive deformation (grain comminution) of the gouge (Bos et al., 2000) and, as a consequence, the growth of the PSZ. This is consistent with the observation of the reduction of the compaction rate and the velocity-strengthening behavior observed at low velocities. Therefore, we suggest three main processes that could lead to the systematic velocity-neutral to -strengthening behavior of both room humidity and wet gouge samples: frictional sliding of grain boundary (i.e., intergranular slip within the PSZ), increasing reduced-size grains by cataclasis, and the development of R- and Y-shears. However, with increasing slip, extreme localization may occur along a principal Y-shear (Marone, 1998), and further experiments are required to investigate this issue.

Water acts as a lubricant in phyllosilicates (Moore & Lockner, 2004; Morrow et al., 2000). For example, Morrow et al. (2000) performed triaxial friction experiments on phyllosilicate-, quartz-, albite-, and calcite-rich gouges under both vacuum-dried and water-saturation conditions. They found that the friction coefficient dropped by 20%–60% for phyllosilicate-rich gouges after the addition of water. The magnitude of friction drops for phyllosilicate grains correlated with the tendency for the phyllosilicate to adsorb interlayer water. Instead, the friction coefficient remained constant for quartz, albite, and graphite regardless of water content. For saturated phyllosilicates, the frictional strength is controlled by the shear through the structured water films formed between the plate surfaces (Moore & Lockner, 2004). In addition, adsorbed water was theoretically proposed to play a role on the friction of a submicron-particle layer (Sammis et al., 2011). Therefore, the presence of water-saturated clay minerals (or submicron particles) could partially reduce the shear strength between grains and is responsible for the difference of overall strength between the room humidity and wet gouge samples.

4.2.2. Enhanced Velocity-Strengthening Behavior at Intermediate Velocities

Although, for a given slip distance and normal stress, the PSZs formed at intermediate velocities are characterized by the same mineral assemblage (Figure 9) and similar microstructures (presence of Y-shears, Figures 6 and 7) as the PSZs formed at low velocities, the PSZs are thicker (Figures 6 and 7). The similar mineral assemblages and microstructures suggest that the deformation mechanisms (grain comminution, intragranular flow, etc.) at low and intermediate velocities are possibly the same, though the weighting by which they formed is slightly different. In addition, amorphization of gouge can be driven by high FWD (Aretusini et al., 2017) but cannot be verified in our results due to the analytical limitation, though all the intensities of XRD peaks at intermediate velocity regime are slightly smaller than the other velocity regimes.

Since quartz grains are larger than clay particles by several order of magnitude, in the case of the WFSD-3 samples (i.e., a quartz-rich mixture with low clay content), the clay minerals would tend to collect in the pores of the matrix framework made by the quartz grains. Therefore, during initial slip, the applied stresses are primarily accommodated by force network chains between the contacting quartz grains, similarly as in the low velocity regime. However, the imposed velocities in the intermediate regime are orders of magnitude higher than in the

low velocity regime. It can be expected that the contacting grains may undergo significant microcracking and comminution due to the shorter contact lifetime at higher strain rate. As a result, the pervasive grain size reduction would occur following the force network chains within the PSZ, the through-going horizontal shear (Y-shear). Therefore, the mechanism operating at low velocity cannot keep with the strain rate at intermediate velocities, and this results in more intense fracturing of the grains and with the increasing development of R-shears, which indicate the formation of intergranular fractures in the gouge layer.

In the intermediate-velocity experiments deformation was localized into both a horizontal Y-shear and an oblique R-shear. R-shear formation and orientation is controlled by the internal friction coefficient of the gouge and may rotate with progressive shear. The shear accommodation by slip along multiple, mutually crosscutting R-P surfaces in the intermediate-velocity regime (Figures 6d and 6e) requires increasing shear stresses with respect to the localized slip along the smooth Y surface of the samples. This could well explain the increase of friction coefficient observed at the intermediate velocities, since sliding along a sub-horizontal shear requires only overcoming of the grain boundary friction, whereas sliding along an obliquely foliated gouge requires dilatation in addition to overcoming grain boundary friction, both contributing to the measured shear stress. As a matter of fact, for similar displacements (ca. 1 m), gouge compaction is higher at low velocities than at intermediate velocities, possibly because of the larger contribution due to gouge dilatancy in the latter velocity regime (compare Figures 4e and 4f with Figures 4g and 4h). As a consequence, cataclasis is still the dominant deformation mechanism, but it requires more shear stress and dilatancy to deform the grains along both Y- and R-shears (here the increase of the friction coefficient and the reduction of the shortening rate compared to the experiments performed in the low velocity regime). The other mechanism, for example, "frictional" grain boundary sliding, is less efficient at the strain rates typical of the intermediate velocity regime.

Similarly, water may act a lubricant and reduce the shear strength between the grains as in the low velocity regime. Because gouge-rich samples have low hydraulic diffusivity which could trap pore fluids pressurized also by compaction during slip, the relatively high velocities applied in the intermediate regime may induce the shear-induced pore fluid pressurization, resulting in a reduction of effective normal stress (Aretusini et al., 2021; Faulkner et al., 2018). Although the pore pressure was neither controlled nor monitored, three lines of evidence suggest that pore fluid pressurization may not be dominant in this regime: (a) the abundant voids of the larger framework quartz grains could allow the pore fluids to drain out efficiently (see also the previous discussion about the lower compaction of the gouges sheared under this regime with respect to those sheared in the low velocity regime); (b) the aforementioned significant microcracking of coarse grains could also be additional fluid path to drain out; and (c) the gradual increase of frictional strength during the experiments, implying the absence of pore fluid pressurization. Therefore, we suggest that, rather than the pressurization of the trapped pore fluids, the water films along the grain boundaries can contribute to the reduction of the bulk frictional strength between the room humidity and wet gouge samples.

4.2.3. Dynamic Weakening Mechanism at High Velocities

Numerous weakening mechanisms derived from rotary shear experiments have been reported (see the summary in Di Toro et al., 2011; Niemeijer et al., 2012). They include flash heating and weakening (Beeler et al., 2008; Goldsby & Tullis, 2011; Rice, 2006), frictional melting lubrication (Di Toro et al., 2006; Hirose & Shimamoto, 2005), silica gel production and lubrication (Di Toro et al., 2004; Goldsby & Tullis, 2002), thermo-mechanical pore fluid pressurization (Aretusini et al., 2021; Brantut & Rice, 2011; Chen et al., 2017; Chen, Yang, Duan, Shimamoto, & Spiers, 2013; Faulkner et al., 2018; Kuo et al., 2021; Rice, 2006; Sibson, 1973; Ujiie & Tsutsumi, 2010; Violay et al., 2015), and powder lubrication (Han et al., 2010, 2011; Reches & Lockner, 2010). Evidence of the presence of amorphous materials (i.e., silica gel or the products derived from frictional melting or clay decomposition) was absent in the sheared gouges based on petrographic microscope, SEM or in situ synchrotron XRD observations. In addition, the modeled temperatures (<450°C and below the melting point of kaolinite, the mineral with the lowest melting temperature in the gouge), together with the lack of phase changes, likely suggest that frictional heating was insufficient to trigger frictional melting (Di Toro et al., 2006; Spray, 2005). Unlike other similar experiments on clay-bearing gouges (e.g., Han et al., 2014), we interpret the lack of evidence of gouge melting (or thermal decomposition) as the result of the short slip distances and duration of the experiments (<1 m and 1 s, respectively). Therefore, processes like frictional melting or fluid pressurization induced by thermo-chemical decomposition of the gouge material seem unlikely to be the cause of the observed slip-weakening behavior, regardless of the humidity conditions. In addition, the PSZs from all the three friction-velocity regimes are

characterized by the abundance of small in grain-size particles. This suggests that powder lubrication may not be active in our case, as the presence of fine grain particles should result in a reduction of the frictional strength with slip independently of the imposed velocities. Below we discuss flash heating and pore fluid pressurization (due to shear-induced compaction and thermal expansion or vaporization of water from mineral surfaces and pores or clay dehydration) as potential weakening mechanisms involved in our experiments.

4.2.3.1. Flash Heating

Because the microstructures of the PSZ are the result of a cumulated deformation, the mechanism responsible for weakening in the initial stage of the experiments remains uncertain. As discussed above, before the initiation of frictional sliding, the applied normal stress is primarily accommodated by force network chains that connect the contacting quartz grains. At the onset of sliding, the high contact stresses and high velocities may drive grain fragmentation but also induce intense and transient heating at grain contacts resulting in dehydration of the clays and melting or thermal softening of the quartz contacts or asperities (Beeler et al., 2008; Rice, 2006). As a result, thermal softening of the contacting asperities likely results in low shear strengths and the associated low macroscopic friction. During flash heating, which is a very short-living (<<ms) mechanism operating at the asperity scale (<<1 mm), the increase of the bulk temperature in the PSZ is extremely difficult to detect with standard analytical techniques (e.g., Niemeijer et al., 2012; Tisato et al., 2012; Figure 8). In addition, with increasing slip distance, other triggered weakening mechanism may overprint the possible evidence for the activation of flash heating (e.g., formation of rods of glass at the microscale: Brantut et al., 2016; Violay et al., 2014). As a result, it is unlikely to recognize the microstructural evidence for flash heating in our experiments. However, since the activation of flash heating and weakening has been documented under both room humidity and wet conditions (Hirose & Bystricky, 2007; Tisato et al., 2012; Violay et al., 2014), we conclude that it might have played a significant role in our experiments, irrespective of the water saturation state.

4.2.3.2. Pore Fluid Pressurization

Information of temperature within the gouge layer (and pore fluid pressure for wet gouges) is required for the investigation of the weakening mechanisms operating at high slip rates. Neither thermocouples nor pore fluid pressure transducers were used, so a thermo-hydro-mechanical (THM) model was developed as a first-order approximation to estimate the local pressure-temperature conditions inside the gouge layer during the experiments (Figure 10).

For the room humidity experiment s1127, because pore fluid pressure evolution can be ignored, we ran a 1D model along the direction orthogonal to the gouge layer which was well developed by Aretusini et al. (2021; Figure 10a). For the wet experiment LHVR1558, we ran a 2D axisymmetric finite element model with the finite element package COMSOL for simulating both temperature and fluid pressure evolution, which is well developed by Chen, Yang, Duan, Shimamoto, and Spiers (2013) (Figure 10d; the same as Figure 11 in Kuo et al., 2021). The heat sources considered in the numerical models were marked in red color in Figures 3c and 3d. All frictional work was assumed to be converted into heat during slip (i.e., τ multiplied by V). For the wet experiment, the heat and thus fluid pressure evolution strongly depend on shear localization. In simulating LHV1558, the frictional heat was assumed to evenly distribute over a 100 μm-thick shear band at one boundary of the simulated gouge layer, mimicking the microstructural observation (as addressed later). The thermal properties (i.e., density, specific heat, and thermal conductivity) of each component of the sample assembly, the transport properties of the gouge layer and the seated porous steel (i.e., porosity, permeability, and specific storage), as well as the water/solid properties (i.e., water and solid compressibility, water and solid expansivity, and water viscosity), were set based on our best knowledge, and was given in Table 3. Besides thermal pressurization, the effect of dilatancy/compaction was also considered for simulating the fluid pressure evolution, based on the observation of changes in axial displacement. To test the parameter sensitivity, we have also varied a few key parameters (e.g., gouge compressibility) to certain extent. Since a large geometry of the sample assembly was simulated, we used a fixed temperature boundary condition (equal to room temperature) and the fluid was assumed to be enclosed within the gouge layer and the seated porous steel (i.e., no flux boundary conditions). For both experiments, we set the initial temperature and pore fluid pressure as 25°C and 1 atm, respectively (Figures 10c and 10g). For s1127, we output temperature from the central node of the SHIVA model (e.g., Aretusini et al., 2021). For LHVR1558, we report the calculated temperature and pore fluid pressure evolution at a radial distance of 8.33 mm from the center of the gouge cylinder (Figure 10g; Kuo et al., 2021). In the developed THM model, we do not consider the effect of grain size reduction by cataclastic process as the microstructures shown below.
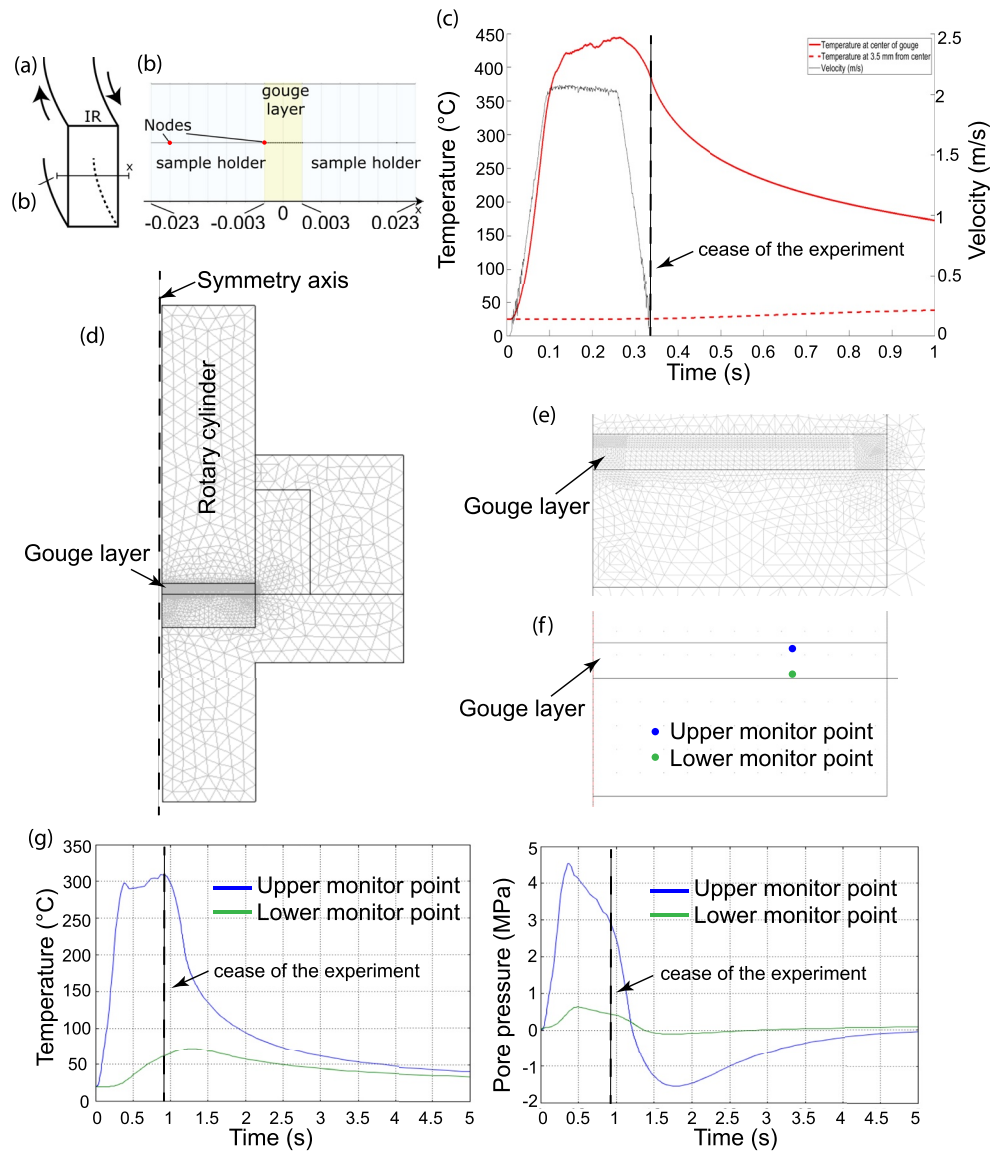
Figure 10. Setup and result of 1D and 2D models. (a) Geometry of the 1D model with respective to the shear direction during the experiments: internal radius (IR). (b) Transect across the gouge layer showing the model domains as well as the mechanical boundary settings. The red circle is the model node at which plots in Figures 4i and 10d are referred to. (c) Result of 1D model. The result is combined with mechanical data in Figure 4i for the discussion. (d) Geometry and material distribution for the 2D model domain as well as the mechanical boundary settings. (e) Mesh and heat source distribution (right hand side). (f) The blue and green circles are the model node at which plots in Figures 4j and 10g are referred to. (g) Results of 2D model. The results are combined with mechanical data in Figure 4j for the discussion.

Our modeling indicates that the room humidity gouge layer rapidly increases to ~400°C in 0.2 m of slip, then gradually reaches a value of ~450°C before deceleration, and eventually slowly decreases at the end of slip (Figures 4i and 10c). On the other hand, the wet gouge layer rapidly increases to a temperature of ~300°C in 0.25 m of slip and reaches a value of ~310°C at the end of slip (Figures 4j and 10g). In addition, the modeled pore fluid pressure rapidly increases to ~4.85 MPa in 0.25 m of slip, gradually decreases to ~3 MPa before deceleration at 0.8 m of slip, and then drops to 0.1 MPa by the end of the experiment (Figures 4j and 10g). In this model the latent heat associated with the liquid-vapor transition was not considered (Chen et al., 2017).

Experiments performed on wet gouges at seismic velocities suggest fault weakening to be controlled by the competition of shear-induced dilatancy and compaction (Proctor et al., 2020). For example, at seismic rates, shear-induced dilatancy may suppress thermal pressurization during the dynamic weakening of faults (Brantut, 2020).

Table 3
Flow and Thermal Properties of Different Materials Used in the LVHR Sample Holder

	Fluid/solid			Porous steel	
β_f	Fluid compressibility	4.3E−10/Pa	ρ	Density	5,000 [kg/m^3]
β_s	Solid compressibility	1.2E−11/Pa	c_p	Specific heat	700 [J/kgK]
η	Fluid viscosity	1.26E−4/Pa	K	Thermal conductivity	10 [W/mK]
α_f	Fluid expansivity	5E−4/K	φ	Porosity	40%
α_s	Solid expansivity	2.2E−5/K	k	Permeability	1e−13 m^2
T$_0$	Room temperature	20°C	S$_s$	Specific storage	$\varphi\beta_f$
p$_0$	Initial pressure	0.1 MPa			
	Brass			**Gouge**	
ρ	Density	8,710[c] [kg/m^3]	ρ	Density	1,231[a] [kg/m^3]
c_p	Specific heat	385 [J/kgK]	c_p	Specific heat	1,269[a] [J/kgK]
K	Thermal conductivity	60[c] [W/mK]	K	Thermal conductivity	1.1[a] [W/mK]
	Stainless		φ	porosity	30%
ρ	Density	8,000[a] [kg/m^3]	k	Permeability	1e−18[b] m^2
c_p	Specific heat	500[a] [J/kgK]	S$_s$	Specific storage	5e−9/Pa
K	Thermal conductivity	16[a] [W/mK]			
	Tungsten carbide				
ρ	Density	15,700[a] [kg/m^3]			
c_p	Specific heat	350[a] [J/kgK]			
K	Thermal conductivity	80[a] [W/mK]			

Note. superscript a is from Aretusini et al. (2019, 2021); superscript b is from Tanikawa et al. (2010); superscript c is from Bossart (2005); the other values are the assumed values from references.

Aretusini et al. (2021), thanks to a dedicated pressure vessel, measured the short-lived pore fluid pressures transients occurring within the gouge layer. They showed the complex evolution of pore fluid pressure during fault slip: shear-induced dilatancy was observed during initial slip acceleration, manifested by a gouge layer thickness increase and pore fluid pressure drop. Then pore fluid pressure increased with slip due to gouge compaction.

The model here proposed for the shearing of wet gouges at seismic velocities (Figure 4j) shows the rapid increase of pore fluid pressure (up to ~4.85 MPa) during the weakening regime. Considering the fact that both mineralogy (low permeability clays) and slip velocity conditions (high slip velocities) of the experiment may drive the gouge sheared at undrained-like conditions, although the gouge layer was allowed to be drained at the boundary condition in our study. It presumably allows to result in an abrupt increase of pore pressure by shear-induced compaction (Kuo et al., 2021). Therefore, the increase of the modeled pore fluid pressure, together with the measured compaction during sliding, was likely as a cause of shear-induced compaction.

Afterward, a gradual decrease of pore fluid pressure with slip correlates with the condition of fluid drainage (i.e., the pressurized fluids moved through the gouge layer and into the fluid outlet). Based on the water phase diagram (Chen et al., 2017; Weatherley & Henley, 2013), the temperatures for water vaporization at 3–4.85 MPa (Figure 4j) are estimated in ~230°C to 260°C. The modeled bulk temperatures for this experiment are about the temperatures required for water vaporization, suggesting that the pore fluids could be in liquid/vapor phase during the weakening regime. If so, pore water begins to vaporize and pore pressure will increase due to a volume expansion of ~1,700 times (0.001 → 1.680 m^3/kg at 100°C) once the temperature reaches the boiling temperature. However, significant dilation of the gouge layer was not observed in our data (Figure 4). Also, our modeling suggests that pore pressure increases faster than temperature at slip initiation; the pore fluid cannot vaporize and be responsible for gouge weakening, even though water vaporization can be triggered by the drop of pore pressure afterward (Chen et al., 2017). Our estimates for high pore fluid pressures are consistent with the recently reported data by Hunfeld et al. (2021) and Aretusini et al. (2021), implying pore fluid pressurization (e.g., mechanical compaction and thermal expansion of pore fluid) as the potential weakening mechanism.

4.3. Implications to the Guanxian-Anxian Fault

Investigating the friction strength and stability in fault gouges and the associated microstructures is crucial to understand individual mechanisms that operated during fault deformation. Our rock friction experiments, spanning a wide range of slip velocities, revealed the frictional behavior of WFSD-3 samples, including slip velocity strengthening at low to intermediate velocities and velocity weakening at high velocities.

Steady state velocity-strengthening behavior under room humidity conditions was observed in a rather large number of experimental data sets (see the detailed summary in Bar-Sinai et al., 2014). In addition, slip velocity-strengthening frictional behavior is known to promote stable slip on faults, to limit the propagation speed of interfacial rupture fronts and to affect the magnitude of slip events (Bar-Sinai et al., 2013, 2014; Bouchbinder et al., 2011; Hawthorne & Rubin, 2013; Kato, 2003; Weeks, 1993), to limit the thickness of the seismogenic zone (Marone & Scholz, 1988), and to control earthquake after slip and stress drops (Marone et al., 1991). Our experimental dataset suggests that the observed enhanced velocity-strengthening frictional behavior of WFSD-3 at intermediate velocities may act as a barrier to slip acceleration and, instead, could result in stable sliding or slow fault rupture (Bar-Sinai et al., 2012). On the other hand, the observed slip weakening at high velocities is similar to the one described in previous studies (Aretusini et al., 2021; Chen et al., 2017; Chen, Yang, Duan, Shimamoto, & Spiers, 2013; Chen, Yang, Yao, Ma, & Shimamoto, 2013; Faulkner et al., 2011; Ferri et al., 2011; Ujiie & Tsutsumi, 2010; Violay et al., 2015). In the WFSD-3 gouges, the dynamic weakening mechanism involves the interplay between flash heating and pore fluid thermo-mechanical pressurization.

The microstructures of the experimental products can be used to indicate where deformation took place, but are of limited use for constraining fault strength due to their similarity. The reduction in grain size of our gouges likely suggests the correlation between the energy dissipation during the experiments and the width of the individual PSZ. Figure 8 shows that the width of PSZ increased with FWD but is independent of FPD. These trends suggest that the processes of mechanical cataclasis were driven by frictional work densities and consequently, control the growth of PSZ. This is consistent with the previous studies on the production by mechanical wear (e.g., the production of size-reduced nano-particles and subsequent solid state amorphization; Aretusini et al., 2017). Meanwhile, the experiments (10 MPa, room humidity and wet conditions, a range of slip velocities and fluid drained conditions) presented here are representative of shallow depths and fluid drainage conditions. Therefore, both the developed correlation between energy dissipation during experiments and the microstructures (the thickness of PSZ) and the reduced grain-sized particles may allow extrapolation of laboratory observation to the observed foliated gouges of GAF (i.e., various grain-sized gouge layers; He et al., 2018), although the activation of pressure solution processes in the gouge reported in He et al. (2018) was not reproduced in this study.

5. Conclusions

We deform room humidity and wet WFSD-3 fault gouges at slip velocities V ranging from 10^{-5} to 2 m/s and normal stresses from 8.5 to 10 MPa. At any imposed slip velocity, the wet gouges have a lower apparent friction coefficient than the room humidity ones. In addition, three friction-velocity regimes are recognized: velocity-neutral to velocity-strengthening regime at low velocities ($V \leq 10^{-2}$ m/s), enhanced velocity-strengthening at intermediate velocities (10^{-2} m/s $< V \leq 10^{-1}$ m/s) and, velocity-weakening at high velocities (10^{-1} m/s $< V$). Microstructural and mineralogical investigations evidence the formation of size-reduced grains (without mineral phase changes) and R- and Y-shears in the PSZ. Regardless of the ambient conditions, the width of PSZ is proportional to the input FWD. Our finding, including the positive relation between FWD and the width of PSZ and the formation of reduced grain-sized particles, may allow the extrapolation of the experimental observations to the observed foliated gouges of GAF. Overall, our results support the hypothesis that the GAF preferentially ruptures through wet fault gouges; however, the enhanced velocity-strengthening regime at intermediate velocities may act as a barrier to slip acceleration during fault rupture propagation.

Data Availability Statement

All the experimental raw data are available in Figshare with the identifier at https://figshare.com/s/dd2aa67ed9caa7b98f1c.

References

Aiyama, K., Mizoguchi, K., Hirano, K., & Takizawa, S. (2019). Effects of sample preparation on the microstructural signatures of faulting in clay-bearing fault gouge. *Journal of Structural Geology*, *126*, 100–108. https://doi.org/10.1016/j.jsg.2019.06.001

Aretusini, S., Meneghini, F., Spagnuolo, E., Harbord, C. W., & Di Toro, G. (2021). Fluid pressurisation and earthquake propagation in the Hikurangi subduction zone. *Nature Communications*, *12*, 2481. https://doi.org/10.1038/s41467-021-22805-w

Aretusini, S., Mittempergher, S., Plümper, O., Spagnuolo, E., Gualtieri, A. F., & Di Toro, G. (2017). Production of nanoparticles during experimental deformation of smectite and implications for seismic slip. *Earth and Planetary Science Letters*, *463*, 221–231. https://doi.org/10.1016/j.epsl.2017.01.048

Aretusini, S., Plümper, O., Spagnuolo, E., & Di Toro, G. (2019). Subseismic to seismic slip in smectite clay nanofoliation. *Journal of Geophysical Research: Solid Earth*, *124*. https://doi.org/10.1029/2019jb017364

Bar-Sinai, Y., Brener, E. A., & Bouchbinder, E. (2012). Slow rupture of frictional interfaces. *Geophysical Research Letters*, *39*(3). https://doi.org/10.1029/2011GL050554

Bar-Sinai, Y., Spatschek, R., Brener, E. A., & Bouchbinder, E. (2013). Instabilities at frictional interfaces: Creep patches, nucleation, and rupture fronts. *Physical Review E*, *88*(6), 060403. https://doi.org/10.1103/PhysRevE.88.060403

Bar-Sinai, Y., Spatschek, R., Brener, E. A., & Bouchbinder, E. (2014). On the velocity-strengthening behavior of dry friction. *Journal of Geophysical Research: Solid Earth*, *119*(3), 1738–1748. https://doi.org/10.1002/2013JB010586

Beeler, N. M., Tullis, T. E., & Goldsby, D. L. (2008). Constitutive relationships and physical basis of fault strength due to flash heating. *Journal of Geophysical Research: Solid Earth*, *113*(B1). https://doi.org/10.1029/2007JB004988

Bos, B., Peach, C. J., & Spiers, C. J. (2000). Frictional-viscous flow of simulated fault gouge caused by the combined effects of phyllosilicates and pressure solution. *Tectonophysics*, *327*(3–4), 173–194. https://doi.org/10.1016/S0040-1951(00)00168-2

Bossart, P. (2005). *Characteristics of the Opalinus Clay at Mont Terri*. Retrieved from http://www.montterri.ch/internet/mont-erri/en/home/geology/key_characteristics.htm

Bouchbinder, E., Brener, E. A., Barel, I., & Urbakh, M. (2011). Slow cracklike dynamics at the onset of frictional sliding. *Physical Review Letters*, *107*(23), 235501. https://doi.org/10.1103/PhysRevLett.107.235501

Boutareaud, S., Wibberley, C. A., Fabbri, O., & Shimamoto, T. (2008). Permeability structure and co-seismic thermal pressurization on fault branches: Insights from the Usukidani Fault, Japan. *Geological Society, London, Special Publications*, *299*(1), 341–361. https://doi.org/10.1144/SP299.20

Brantut, N. (2020). Dilatancy-induced fluid pressure drop during dynamic rupture: Direct experimental evidence and consequences for earthquake dynamics. *Earth and Planetary Science Letters*, *538*, 116179. https://doi.org/10.1016/j.epsl.2020.116179

Brantut, N., Passelègue, F. X., Deldicque, D., Rouzaud, J.-N., & Schubnel, A. (2016). Dynamic weakening and amorphization in serpentinite during laboratory earthquakes. *Geology*, *44*, 607–610. https://doi.org/10.1130/G37932.1

Brantut, N., & Rice, J. R. (2011). How pore fluid pressurization influences crack tip processes during dynamic rupture. *Geophysical Research Letters*, *38*(24), L24314. https://doi.org/10.1029/2011GL050044

Brown, K. M., Kopf, A., Underwood, M. B., & Weinberger, J. L. (2003). Compositional and fluid pressure controls on the state of stress on the Nankai subduction thrust: A weak plate boundary. *Earth and Planetary Science Letters*, *214*(3–4), 589–603. https://doi.org/10.1016/S0012-821X(03)00388-1

Chen, J., Niemeijer, A., Yao, L., & Ma, S. (2017). Water vaporization promotes coseismic fluid pressurization and buffers temperature rise. *Geophysical Research Letters*, *44*(5), 2177–2185. https://doi.org/10.1002/2016GL071932

Chen, J., Yang, X., Duan, Q., Shimamoto, T., & Spiers, C. J. (2013). Importance of thermochemical pressurization in the dynamic weakening of the Longmenshan Fault during the 2008 Wenchuan earthquake: Inferences from experiments and modeling. *Journal of Geophysical Research: Solid Earth*, *118*(8), 4145–4169. https://doi.org/10.1002/jgrb.50260

Chen, J., Yang, X., Yao, L., Ma, S., & Shimamoto, T. (2013). Frictional and transport properties of the 2008 Wenchuan earthquake Fault zone: Implications for coseismic slip-weakening mechanisms. *Tectonophysics*, *603*, 237–256. https://doi.org/10.1016/j.tecto.2013.05.035

Di Toro, G., Goldsby, D. L., & Tullis, T. E. (2004). Friction falls towards zero in quartz rock as slip velocity approaches seismic rates. *Nature*, *427*(6973), 436–439. https://doi.org/10.1038/nature02249

Di Toro, G., Han, R., Hirose, T., De Paola, N., Nielsen, S., Mizoguchi, K., et al. (2011). Fault lubrication during earthquakes. *Nature*, *471*(7339), 494–498. https://doi.org/10.1038/nature09838

Di Toro, G., Hirose, T., Nielsen, S., Pennacchioni, G., & Shimamoto, T. (2006). Natural and experimental evidence of melt lubrication of faults during earthquakes. *Science*, *311*(5761), 647–649. https://doi.org/10.1126/science.1121012

Di Toro, G., Niemeijer, A., Tripoli, A., Nielsen, S., Di Felice, F., Scarlato, P., et al. (2010). From field geology to earthquake simulation: A new state-of-the-art tool to investigate rock friction during the seismic cycle (SHIVA). *Rendiconti Lincei*, *21*(1), 95–114. https://doi.org/10.1007/s12210-010-0097-x

Faulkner, D. R., Mitchell, T. M., Behnsen, J., Hirose, T., & Shimamoto, T. (2011). Stuck in the mud? Earthquake nucleation and propagation through accretionary forearcs. *Geophysical Research Letters*, *38*, L18303. https://doi.org/10.1029/2011GL048552

Faulkner, D. R., Sanchez-Roa, C., Boulton, C., & denHartog, S. A. M. (2018). Pore-fluid pressure development in compacting fault gouge in theory, experiments, and nature. *Journal of Geophysical Research: Solid Earth*, *123*(1), 226–241. https://doi.org/10.1002/2017jb015130

Ferri, F., Di Toro, G., Hirose, T., Han, R., Noda, H., Shimamoto, T., et al. (2011). Low-to high-velocity frictional properties of the clay-rich gouges from the slipping zone of the 1963 Vaiont slide, northern Italy. *Journal of Geophysical Research: Solid Earth*, *116*(B9). https://doi.org/10.1029/2011JB008338

Goldsby, D. L., & Tullis, T. E. (2002). Low frictional strength of quartz rocks at subseismic slip rates. *Geophysical Research Letters*, *29*(17), 25-1–25-4. https://doi.org/10.1029/2002GL015240

Goldsby, D. L., & Tullis, T. E. (2011). Flash heating leads to low frictional strength of crustal rocks at earthquake slip rates. *Science*, *334*(6053), 216–218. https://doi.org/10.1126/science.1207902

Han, R., Hirose, T., Jeong, G. Y., Ando, J. I., & Mukoyoshi, H. (2014). Frictional melting of clayey gouge during seismic fault slip: Experimental observation and implications. *Geophysical Research Letters*, *41*(15), 5457–5466. https://doi.org/10.1002/2014GL061246

Han, R., Hirose, T., & Shimamoto, T. (2010). Strong velocity weakening and powder lubrication of simulated carbonate faults at seismic slip rates. *Journal of Geophysical Research: Solid Earth*, *115*(B3). https://doi.org/10.1029/2008JB006136

Han, R., Hirose, T., Shimamoto, T., Lee, Y., & Ando, J. I. (2011). Granular nanoparticles lubricate faults during seismic slip. *Geology*, *39*(6), 599–602. https://doi.org/10.1130/G31842.1

Hawthorne, J. C., & Rubin, A. M. (2013). Laterally propagating slow slip events in a rate and state friction model with a velocity-weakening to velocity-strengthening transition. *Journal of Geophysical Research: Solid Earth*, *118*(7), 3785–3808. https://doi.org/10.1002/jgrb.50261

He, X. L., Li, H. B., Wang, H., Zhang, L., Xu, Z. Q., & Si, J. L. (2018). Creeping along the Guanxian-Anxian fault of the 2008 Mw 7.9 Wenchuan earthquake in the Longmen Shan, China. *Tectonics*, *37*(7), 2124–2141. https://doi.org/10.1029/2017TC004820

Hirose, T., & Bystricky, M. (2007). Extreme dynamic weakening of faults during dehydration by coseismic shear heating. *Geophysical Research Letters*, *34*(14). https://doi.org/10.1029/2007GL030049

Hirose, T., & Shimamoto, T. (2005). Growth of molten zone as a mechanism of slip weakening of simulated faults in gabbro during frictional melting. *Journal of Geophysical Research: Solid Earth*, *110*(B5). https://doi.org/10.1029/2004JB003207

Hou, L., Ma, S., Shimamoto, T., Chen, J., Yao, L., Yang, X., & Okimura, Y. (2012). Internal structures and high-velocity frictional properties of a bedding-parallel carbonate fault at Xiaojiaqiao outcrop activated by the 2008 Wenchuan earthquake. *Earthquake Science*, *25*, 197–217. https://doi.org/10.1007/s11589-012-0846-2

Hunfeld, L. B., Chen, J., Niemeijer, A. R., Ma, S., & Spiers, C. J. (2021). Seismic slip-pulse experiments simulate induced earthquake rupture in the Groningen gas field. *Geophysical Research Letters*, *48*(11), e2021GL092417. https://doi.org/10.1029/2021GL092417

Hung, C. C., Kuo, L. W., Spagnuolo, E., Wang, C. C., Di Toro, G., Wu, W. J., et al. (2019). Grain fragmentation and frictional melting during initial experimental deformation and implications for seismic slip at shallow depths. *Journal of Geophysical Research: Solid Earth*, *124*(11), 11150–11169. https://doi.org/10.1029/2019JB017905

Ikari, M. J., Saffer, D. M., & Marone, C. (2007). Effect of hydration state on the frictional properties of montmorillonite-based fault gouge. *Journal of Geophysical Research: Solid Earth*, *112*(B6), B06423. https://doi.org/10.1029/2006JB004748

Ikari, M. J., Saffer, D. M., & Marone, C. (2009). Frictional and hydrologic properties of clay-rich fault gouge. *Journal of Geophysical Research: Solid Earth*, *114*(B5). https://doi.org/10.1029/2008JB006089

Kato, N. (2003). A possible model for large preseismic slip on a deeper extension of a seismic rupture plane. *Earth and Planetary Science Letters*, *216*(1–2), 17–25. https://doi.org/10.1016/S0012-821X(03)00483-7

Kuo, L. W., Di Felice, F., Spagnuolo, E., Di Toro, G., Song, S. R., Aretusini, S., et al. (2017). Fault gouge graphitization as evidence of past seismic slip. *Geology*, *45*(11), 979–982. https://doi.org/10.1130/G39295.1

Kuo, L. W., Hsiao, H. C., Song, S. R., Sheu, H. S., & Suppe, J. (2014). Coseismic thickness of principal slip zone from the Taiwan Chelungpu fault Drilling Project-A (TCDP-A) and correlated fracture energy. *Tectonophysics*, *619*, 29–35. https://doi.org/10.1016/j.tecto.2013.07.006

Kuo, L. W., Li, H., Smith, S., Di Toro, G., Suppe, J., Song, S. R., et al. (2014). Gouge graphitization and dynamic fault weakening during the 2008 Mw 7.9 Wenchuan earthquake. *Geology*, *42*, 47–50. https://doi.org/10.1130/G34862.1

Kuo, L. W., Song, Y. F., Yang, C. M., Song, S. R., Wang, C. C., Dong, J. J., et al. (2015). Ultrafine spherical quartz formation during seismic fault slip: Natural and experimental evidence and its implications. *Tectonophysics*, *664*, 98–108. https://doi.org/10.1016/j.tecto.2015.09.008

Kuo, L. W., Wu, W. J., Kuo, C. W., Smith, S. A., Lin, W. T., Wu, W. H., & Huang, Y. H. (2021). Frictional strength and fluidization of water-saturated kaolinite gouges at seismic slip velocities. *Journal of Structural Geology*, *150*, 104419. https://doi.org/10.1016/j.jsg.2021.104419

Li, H., Wang, H., Xu, Z., Si, J., Pei, J., Li, T., et al. (2013). Characteristics of the fault-related rocks, fault zones and the principal slip zone in the Wenchuan Earthquake Fault Scientific Drilling project hole-1 (WFSD-1). *Tectonophysics*, *584*, 23–42. https://doi.org/10.1016/j.tecto.2012.08.021

Li, H., Wang, H., Yang, G., Xu, Z., Li, T., Si, J., et al. (2016). Lithological and structural characterization of the Longmen Shan fault belt from the 3rd hole of the Wenchuan Earthquake Fault Scientific Drilling project (WFSD-3). *International Journal of Earth Sciences*, *105*(8), 2253–2272. https://doi.org/10.1007/s00531-015-1285-9

Li, H., Xue, L., Brodsky, E. E., Mori, J. J., Fulton, P. M., Wang, H., et al. (2016). Long-term temperature records following the Mw 7.9 Wencuhan (China) earthquake are consistent with low friction. *Geology*, *43*, 163–166. https://doi.org/10.1130/G35515.1

Liu-Zeng, J., Zhang, Z., Wen, L., Tapponnier, P., Sun, J., Xing, X., et al. (2009). Co-seismic ruptures of the 12 May 2008, Ms 8.0 Wenchuan earthquake, Sichuan: East–west crustal shortening on oblique, parallel thrusts along the eastern edge of Tibet. *Earth and Planetary Science Letters*, *286*(3–4), 355–370. https://doi.org/10.1016/j.epsl.2009.07.017

Logan, J. M., Dengo, C. A., Higgs, N. G., & Wang, Z. Z. (1992). Fabrics of experimental fault zones: Their development and relationship to mechanical behaviour. *International Geophysics*, *51*, 33–67. https://doi.org/10.1016/S0074-6142(08)62814-4

Ma, S., Shimamoto, T., Yao, L., Togo, T., & Kitajima, H. (2014). A rotary-shear low to high-velocity friction apparatus in Beijing to study rock friction at plate to seismic slip rates. *Earthquake Science*, *27*(5), 469–497. https://doi.org/10.1007/s11589-014-0097-5

Marone, C. J. (1998). Laboratory-derived friction laws and their application to seismic faulting. *Annual Review of Earth and Planetary Sciences*, *26*(1), 643–696. https://doi.org/10.1146/annurev.earth.26.1.643

Marone, C. J., & Scholz, C. H. (1988). The depth of seismic faulting and the upper transition from stable to unstable slip regimes. *Geophysical Research Letters*, *15*(6), 621–624. https://doi.org/10.1029/GL015i006p00621

Marone, C. J., Scholtz, C. H., & Bilham, R. (1991). On the mechanics of earthquake afterslip. *Journal of Geophysical Research: Solid Earth*, *96*(B5), 8441–8452. https://doi.org/10.1029/91JB00275

Mizoguchi, K., Hirose, T., Shimamoto, T., & Fukuyama, E. (2007). Reconstruction of seismic faulting by high-velocity friction experiments: An example of the 1995 Kobe earthquake. *Geophysical Research Letters*, *34*(1). https://doi.org/10.1029/2006GL027931

Mizoguchi, K., Takahashi, M., Tanikawa, W., Masuda, K., Song, S. R., & Soh, W. (2008). Frictional strength of fault gouge in Taiwan Chelungpu fault obtained from TCDP Hole B. *Tectonophysics*, *460*(1–4), 198–205. https://doi.org/10.1016/j.tecto.2008.08.009

Moore, D. E., & Lockner, D. A. (2004). Crystallographic controls on the frictional behavior of dry and water-saturated sheet structure minerals. *Journal of Geophysical Research: Solid Earth*, *109*(B3). https://doi.org/10.1029/2003JB002582

Morrow, C. A., Moore, D. E., & Lockner, D. A. (2000). The effect of mineral bond strength and adsorbed water on fault gouge frictional strength. *Geophysical Research Letters*, *27*(6), 815–818. https://doi.org/10.1029/1999GL008401

Niemeijer, A., Di Toro, G., Griffith, W. A., Bistacchi, A., Smith, S. A., & Nielsen, S. (2012). Inferring earthquake physics and chemistry using an integrated field and laboratory approach. *Journal of Structural Geology*, *39*, 2–36. https://doi.org/10.1016/j.jsg.2012.02.018

Niemeijer, A., Marone, C., & Elsworth, D. (2010). Frictional strength and strain weakening in simulated fault gouge: Competition between geometrical weakening and chemical strengthening. *Journal of Geophysical Research: Solid Earth*, *115*(B10). https://doi.org/10.1029/2009JB000838

Proctor, B., Lockner, D. A., Kilgore, B. D., Mitchell, T. M., & Beeler, N. M. (2020). Direct evidence for fluid pressure, dilatancy, and compaction affecting slip in isolated faults. *Geophysical Research Letters*, *47*(16), e2019GL086767. https://doi.org/10.1029/2019GL086767

Reches, Z. E., & Lockner, D. A. (2010). Fault weakening and earthquake instability by powder lubrication. *Nature*, *467*(7314), 452–455. https://doi.org/10.1038/nature09348

Remitti, F., Smith, S. A. F., Mittempergher, S., Gualtieri, A. F., & Di Toro, G. (2015). Frictional properties of fault zone gouges from the J-FAST drilling project (Mw 9.0 2011 Tohoku-Oki earthquake). *Geophysical Research Letters*, *42*(8), 2691–2699. https://doi.org/10.1002/2015GL063507

Rempe, M., Smith, S. A. F., Hirose, T., & Di Toro, G. (2017). The effect of water on strain localization in calcite fault gouge sheared at seismic slip rates. *Journal of Structural Geology*, *97*, 104–117. https://doi.org/10.1016/j.jsg.2017.02.007

Rice, J. R. (2006). Heating and weakening of faults during earthquake slip. *Journal of Geophysical Research: Solid Earth*, *111*(B5). https://doi.org/10.1029/2005JB004006

Sammis, C. G., Lockner, D. A., & Reches, Z. (2011). The role of adsorbed water on the friction of a layer of submicron particles. *Pure and Applied Geophysics*, *168*, 2325–2334. https://doi.org/10.1007/s00024-011-0324-0

Schuttlefield, J. D., Cox, D., & Grassian, V. H. (2007). An investigation of water uptake on clays minerals using ATR-FTIR spectroscopy coupled with quartz crystal microbalance measurements. *Journal of Geophysical Research: Atmospheres*, *112*(D21). https://doi.org/10.1029/2007JD008973

Sibson, R. H. (1973). Interactions between temperature and pore-fluid pressure during earthquake faulting and a mechanism for partial or total stress relief. *Nature; Physical Science*, *243*(126), 66–68. https://doi.org/10.1038/physci243066a0

Smith, S. A. F., Di Toro, G., Kim, S., Ree, J. H., Nielsen, S., Billi, A., & Spiess, R. (2013). Coseismic recrystallization during shallow earthquake slip. *Geology*, *41*(1), 63–66. https://doi.org/10.1130/G33588.1

Sone, H., & Shimamoto, T. (2009). Frictional resistance of faults during accelerating and decelerating earthquake slip. *Nature Geoscience*, *2*(10), 705–708. https://doi.org/10.1038/ngeo637

Spray, J. G. (2005). Evidence for melt lubrication during large earthquakes. *Geophysical Research Letters*, *32*(7). https://doi.org/10.1029/2004GL022293

Tanikawa, W., Sakaguchi, M., Tadai, O., & Hirose, T. (2010). Influence of fault slip rate on shear-induced permeability. *Journal of Geophysical Research*, *115*, B07412. https://doi.org/10.1029/2009JB007013

Tanikawa, W., & Shimamoto, T. (2009). Frictional and transport properties of the Chelungpu fault from shallow borehole data and their correlation with seismic behavior during the 1999 Chi-Chi earthquake. *Journal of Geophysical Research: Solid Earth*, *114*(B1). https://doi.org/10.1029/2008JB005750

Tembe, S., Lockner, D. A., & Wong, T. F. (2010). Effect of clay content and mineralogy on frictional sliding behavior of simulated gouges: Binary and ternary mixtures of quartz, illite, and montmorillonite. *Journal of Geophysical Research: Solid Earth*, *115*(B3). https://doi.org/10.1029/2009JB006383

Tisato, N., Di Toro, G., De Rossi, N., Quaresimin, M., & Candela, T. (2012). Experimental investigation of flash weakening in limestone. *Journal of Structural Geology*, *38*, 183–199. https://doi.org/10.1016/j.jsg.2011.11.017

Togo, T., Shimamoto, T., Ma, S., & Hirose, T. (2011). High-velocity frictional behavior of Longmenshan fault gouge from Hongkou outcrop and its implications for dynamic weakening of fault during the 2008 Wenchuan earthquake. *Earthquake Science*, *24*(3), 267–281. https://doi.org/10.1007/s11589-011-0790-6

Togo, T., Yao, L., Ma, S., & Shimamoto, T. (2016). High-velocity frictional strength of Longmenshan fault gouge and its comparison with an estimate of friction from the temperature anomaly in WFSD-1 drill hole. *Journal of Geophysical Research: Solid Earth*, *121*(7), 5328–5348. https://doi.org/10.1002/2016JB012880

Tsutsumi, A., & Shimamoto, T. (1997). High-velocity frictional properties of gabbro. *Geophysical Research Letters*, *24*(6), 699–702. https://doi.org/10.1029/97GL00503

Ujiie, K., & Tsutsumi, A. (2010). High-velocity frictional properties of clay-rich fault gouge in a megasplay fault zone, Nankai subduction zone. *Geophysical Research Letters*, *37*(24). https://doi.org/10.1029/2010GL046002

Violay, M., Di Toro, G., Nielsen, S., Spagnuolo, E., & Burg, J. P. (2015). Thermo-mechanical pressurization of experimental faults in cohesive rocks during seismic slip. *Earth and Planetary Science Letters*, *429*, 1–10. https://doi.org/10.1016/j.epsl.2015.07.054

Violay, M., Nielsen, S., Gibert, B., Spagnuolo, E., Cavallo, A., Azais, P., et al. (2014). Effect of water on the frictional behavior of cohesive rocks during earthquakes. *Geology*, *42*(1), 27–30. https://doi.org/10.1130/G34916.1

Weatherley, D. K., & Henley, R. W. (2013). Flash vaporization during earthquakes evidenced by gold deposits. *Nature Geoscience*, *6*(4), 294–298. https://doi.org/10.1038/ngeo1759

Weeks, J. D. (1993). Constitutive laws for high-velocity frictional sliding and their influence on stress drop during unstable slip. *Journal of Geophysical ResearchSolid E*, *98*(B10), 17637–17648. https://doi.org/10.1029/93JB00356

Wu, W. J., Kuo, L. W., Ku, C. S., Chiang, C. Y., Sheu, H. S., Aprilniadi, T. D., & Dong, J. J. (2020). Mixed-mode formation of amorphous materials in the creeping zone of the Chihshang Fault, Taiwan, and implications for deformation style. *Journal of Geophysical Research: Solid Earth*, *125*(6), e2020JB019862. https://doi.org/10.1029/2020JB019862

Xu, X., Wen, X., Yu, G., Chen, G., Klinger, Y., Hubbard, J., & Shaw, J., (2009). Coseismic reverse- and oblique-slip surface faulting generated by the 2008 Mw7.9 Wenchuan earthquake. *China: Geology*, *37*, 515–518. https://doi.org/10.1130/G25462A.1

Yao, L., Ma, S., Shimamoto, T., & Togo, T. (2013). Structures and high-velocity frictional properties of the Pingxi fault zone in the Longmenshan fault system, Sichuan, China, activated during the 2008 Wenchuan earthquake. *Tectonophysics*, *599*, 135–156. https://doi.org/10.1016/j.tecto.2013.04.011

Yao, L., Shimamoto, T., Ma, S., Han, R., & Mizoguchi, K. (2013). Rapid postseismic strength recovery of Pingxi fault gouge from the Longmenshan fault system: Experiments and implications for the mechanisms of high-velocity weakening of faults. *Journal of Geophysical Research: Solid Earth*, *118*(8), 4547–4563. https://doi.org/10.1002/jgrb.50308

Zhang, P. Z., Wen, X. Z., Shen, Z. K., & Chen, J. H. (2010). Oblique, high-angle, listric-reverse faulting and associated development of strain: The Wenchuan earthquake of May 12, 2008, Sichuan, China. *Annual Review of Earth and Planetary Sciences*, *38*, 353–382. https://doi.org/10.1146/annurev-earth-040809-152602

Zhang, Y., Feng, W., Xu, L., Zhou, C., & Chen, Y. (2009). Spatio-temporal rupture process of the 2008 great Wenchuan earthquake. *Science in China Series D: Earth Sciences*, *52*(2), 145–154. https://doi.org/10.1007/s11430-008-0148-7